TRANSITION METALS IN THE RODENT BRAIN

MEASUREMENT OF TRANSITION METALS IN THE RODENT BRAIN USING X-RAY FLUORESCENCE AND NEUTRON ACTIVATION ANALYSIS

By

NATALIYA MOLDOVAN, BSC (HONS)

A Thesis

Submitted to the School of Graduate Studies

in Partial Fulfilment of the Requirements

for the Degree

Master of Science

McMaster University

MASTER OF SCIENCE (2012) McMaster University

Medical Physics & Applied Radiation Sciences Hamilton, Ontario

TITLE: Measurement of Transition Metals in the Rodent Brain using X-ray Fluorescence and Neutron Activation Analysis

AUTHOR: Nataliya Moldovan,
BSc Hons (University of Western Ontario)

SUPERVISORS: Dr. Nicholas Bock
Dr. Michael Farquharson

NUMBER OF PAGES: xiii, 70

Abstract

Transition metals, such as iron, manganese, and copper are essential in the development and function of biological systems. However, disrupted levels of transition metals are highly cytotoxic, and metal homeostasis is strictly maintained in cells under normal conditions. The neuropathology of several brain disorders, such as Alzheimer's disease and Parkinson's disease has been linked to altered metal levels. This work focused on the measurement of iron, manganese, and copper, with the aim of better elucidating their role in brain disease.

Two experiments were carried out in C57Bl/6 mice looking at metal homeostasis: *1.* following manganese injections typically administered in manganese-enhanced MRI animal studies, and *2.* following copper deficiency in a cuprizone model of demyelination. Metal measurements were made in the brain and visceral organs using X-ray fluorescence to measure iron and copper concentrations, and neutron activation analysis to measure manganese concentrations.

In the MEMRI study in this work, in addition to the expected manganese concentration increases in brain regions following high-dose manganese injections, a statistically significant decrease in iron concentration in the thalamus was found. This change in iron levels in the thalamus following manganese injections should serve as a caution that care should be taken when interpreting signal changes in brain regions.

The cuprizone study in this thesis confirmed that copper levels are reduced following cuprizone administration in C57Bl/6 mice. Surprisingly, manganese concentrations were significantly higher in several brain regions that are known to demyelinate in this model but not copper or iron. The mechanism of cuprizone toxicity was related to manganese neurotoxicity that may contribute to demyelination through activation of microglia and astrocytes, as well as disruption of astrocytes themselves.

The measurements developed in this work have many applications in neurological diseases in which altered metal levels have been implicated, and these techniques can be used not only in rodent but in human tissue.

Acknowledgements

I would like to take this opportunity to thank a number of people for their continuous help throughout this research process. Firstly, I would like to thank my research supervisor Dr. Nicholas Bock for his excellent guidance with the research experiments and animal work. I would also like to thank my co-supervisor Dr. Michael Farquharson for his expertise in x-ray fluorescence and Alia Al-Ebraheem for her efforts to teach and provide assistance with this technique. Next, I would like to thank Raina Park for her contributions to this research project in neutron activation analysis measurements. Thank you to my supervisory committee, Dr. Nicholas Bock, Dr. Michael Farquharson and Dr. John Valliant, for their great suggestions and discussions during our meetings. Last but definitely not least, I would like to thank my parents, Olena and Anatoliy and my brother, Artem, for their support and optimism. A very special thank you goes to my twin sister, Sasha, for always being there for me.

Table of Contents

Chapter 5 – Future Works

List of Figures

List of Tables

List of Abbreviations and Symbols

Mn – manganese

Mn^{2+} – divalent manganese ion

Cu – copper

Cu^{2+} – divalent copper ion

Fe – iron

Fe^{3+} – trivalent iron ion

Na^{+} – sodium ion

K^{+} – potassium ion

ppm – parts per million

MS – multiple sclerosis

XRF – x-ray fluorescence

SDD – silicon drift detector

NAA – neutron activation analysis

CNAA – centre for neutron activation analysis

HPGe – high purity germanium

MCA – multichannel analyzer

MNR – McMaster nuclear reactor

MRI – magnetic resonance imaging

MEMRI – manganese-enhanced magnetic resonance imaging

T_1 – longitudinal relaxation time

T_2 – transverse relaxation time

R_1 – longitudinal relaxation rate

R_2 – transverse relaxation rate

$\mathrm{R}_{1\text{ or }2}(0)$ – relaxation of a water solution without paramagnetic ions

$\mathrm{r}_{1,2}$ – relaxivity of a paramagnetic ion

$[\mathrm{ion}]$ – concentration of a paramagnetic ion

CNS – central nervous system

ATP – adenosine triphosphate

SOD – superoxide dismutase

BBB – blood brain barrier

BCB – blood cerebrospinal fluid barrier

TfR – transferrin

DMT-1 – divalent metal transporter 1

Ctr-1– copper transporter 1

Z – atomic number

A – atomic mass

n – neutron

γ – gamma photon

μ – mass attenuation coefficient

E_e – energy of photoelectron

E_γ – incident photon energy

$E_{\gamma'}$ – scattered photon energy

KE_e – kinetic energy of recoil electron

E_b – binding energy of photoelectron

θ – scattering angle

$m_e c^2$ – electron rest mass energy

K_α – x-ray produced in L→K electron transition

K_β – x-ray produced in M→K electron transition

ω_K – K fluorescence yield

n_K – number of K_α x-rays emitted

N_K – number of vacancies created in K shell

F – fraction of photons

ρ – sample density

x – sample thickness

R – count rate

ε – absolute detector efficiency

γ – absolute gamma-ray abundance

φ – neutron flux

σ – neutron capture cross-section

λ – decay constant

t_i – irradiation time

t_d – decay time

A_{sample} – peak area of gamma ray of a specific energy in the sample

$A_{standard}$ – peak area of gamma ray of a specific energy in the standard

N_{sample} – amount of nuclide activated in the sample

$N_{standard}$ – amount of nuclide activated in the standard

Declaration of Academic Achievement

This research work was completed under the supervision of Dr. N. Bock and Dr. M. Farquharson with help from colleagues in their laboratories. My contributions to the original research in this thesis consisted of coordinating and running MEMRI and cuprizone experiments including animal handling, sample preparation, sample measurements, and complete data analysis. The following assistance was received during the MEMRI experiment - help from Alia Al-Ebraheem with XRF measurements and Nelson Miksys with NAA measurements. A summer student, Raina Park, also made NAA measurement contributions under my supervision.

Chapter 1 – Introduction

1.1 Importance of Transition Metals in Brain Function

Transition metals, such as iron, manganese, and copper are essential in the development and function of biological systems, having unique chemical properties which allow them to perform biochemical activities by participating in reduction-oxidation (redox) reactions. It is important, however, that metal homeostasis is strictly maintained in cells. If levels fall too low, the function of the cell will be disrupted, as transition metals are essential in several key metabolic enzymes. If levels are too high, the same chemical properties that make transition metals useful in enzymes can cause oxidative damage to cells. Cytotoxicity of transition metals in the central nervous system (CNS) is thought to result in damage to neurons and glial cells through oxidative damage, cumulating in neurological disease. This work focuses on the measurement of the transition metals iron, manganese, and copper, with the aim of better elucidating their role in brain disease. Two disorders are specifically investigated: manganism, caused by an overexposure to manganese; and demyelination following prolonged exposure to the copper chelator cuprizone, which is a model of multiple sclerosis (MS). Outside of these disorders, disrupted metal levels have been noted in major neurological diseases such as Alzheimer's and Parkinson's. Since measuring metal levels in fresh brain tissue samples is technically difficult, methods such as the ones demonstrated in this thesis are necessary to obtain better data on how metal levels are altered in brain disease.

1.1.1 Functions of Transition Metals in the Brain

Transition metals perform a wide range of biological functions in the brain. A common feature is their ability to exist in a variety of oxidation states and participate in redox reactions; thus copper, iron, and manganese are all catalytically active metals in a class of enzymes that sequester free radicals. It is useful to look at the common and varying functions of transition metals in the brain to better understand what mechanisms are disrupted in metal dyshomeostasis and how this may lead to cell death in diseases of the CNS.

Iron has many important functions in the CNS as a cofactor of metalloenzymes, participating in oxygen transport, nitric oxide metabolism, and oxidative phosphorylation (Donnelly, Xiao, & Wedd, 2007). Generally, iron also maintains the oxygen levels in the brain as a component of hemoglobin. Iron is a cofactor in enzymes involved in ATP synthesis, as well as synthesis of amine neurotransmitters in the brain and plays a critical role in myelin production (Beard, Connor, & Jones, 1993).

Manganese is present in all mammalian tissues and is essential for normal immune function, blood clotting, bone growth, and regulation of blood sugar. On the cellular level, manganese is needed for oxidative cellular respiration, reproduction, digestion, and free radical defense. Manganese is a co-factor of several important metalloenzymes which function in the production of ATP via gluconeogenesis, regulation of ammonia levels, and free radical sequestering (Aschner, Erikson, & Dorman, 2005). Most notably, manganese superoxide dismutases (MnSODs) are manganese containing enzymes that function to sequester the free radical superoxide by converting it into oxygen and hydrogen peroxide (Abreu & Cabelli, 2010).

Copper functions as part of many enzymes in cellular metabolic processes. It is essential for cellular respiration as a cofactor in cytochrome c oxidase and iron oxidation through ferroxidase activity of ceruloplasmin and hephaestin. Copper also plays a role in norepinephrine neurotransmitter synthesis, antioxidant defense, peptide amidation, and connective tissue formation (Madsen & Gitlin, 2007). Similar to manganese, copper functions in dismutation of superoxide by another group of SOD enzymes that contain copper or zinc as co-factors- CuZnSODs (Abreu & Cabelli, 2010).

1.1.2 Uptake and Transport of Transition Metals in the Brain

Owing to their strong potential to cause oxidative damage, transition metals are always transported and stored by associated chaperone proteins in biological systems. Transport into the brain is a unique case, because of the presence of the blood-brain-barrier (BBB) that only allows the passage of select molecules and proteins into the sensitive brain tissue. Transition metals may share transport mechanisms because they have similar chemistry and an understanding of how these

pathways operate is important to understand how transition metal deficiency or over-exposure can occur in the brain.

Iron is abundant in various types of cells in the CNS but the highest concentration is found in astrocytes – a class of glial cells, which are the cells that support neurons in the brain. Thus, astrocytes are thought to function in iron storage and regulation in the CNS (Madsen & Gitlin, 2007). Iron is actively transported into the brain through the blood-brain barrier and the brain-cerebrospinal fluid barrier (BCB) by a protein called transferrin (Madsen & Gitlin, 2007). In the brain, iron can enter cells via two pathways regulated by the transferrin receptor (TfR) and divalent metal transporter-1 (DMT-1) respectively. Once inside the cell, iron is stored bound to a protein called ferritin.

Similar to iron, manganese is transported into the brain across the BBB and BCB; but manganese can also enter the CNS directly following inhalation (Erikson, Thompson, Aschner, & Aschner, 2007). Transport across the brain-cerebrospinal fluid barrier increases when plasma levels of manganese rise (Normandin et al., 2004). Cellular manganese transport involves the same two pathways as iron – TfR and DMT-1 (Aschner et al., 2005), with other protein channels implicated as well. The exact mechanism of manganese distribution across the brain is unclear but studies have demonstrated redistribution via axonal transport of manganese between neurons leading to heterogeneous uptake patterns (Aschner et al., 2005). The intracellular site of manganese storage is the mitochondria.

Copper transport across the BBB and BCB regulates the concentration of copper in the CNS and involves the copper transporter-1 (Ctr-1) and again the DMT-1 protein (Arredondo & Nunez , 2005). As with other transition metals, free copper ions are toxic to cells and inside the cell copper is stored as Cu-metallothionein; incorporated into cytochrome c oxidase in the mitochondria; incorporated into CuZnSOD; or transported to the golgi network for efflux (Madsen & Gitlin, 2007; Zheng & Monnot, 2012). In the brain, cellular copper homeostasis is largely regulated by the transporting ATPases – MNK and WND, while in the liver only WND is expressed. Both MNK and WND are localized to the Golgi body where they also function in copper transport for processing of enzymes requiring copper as a co-factor (Arredondo & Nunez , 2005). However, with

increasing intracellular levels of copper, MNK and WND traffic copper to the plasma membrane for export out of the cell to prevent excess copper accumulation (Zheng & Monnot, 2012).

1.2 Transition Metal Homeostasis in the Brain

As mentioned earlier, transition metal homeostasis in the brain is tightly regulated, and it is likely that metal-related brain disease occurs when this homeostasis is disrupted.

1.2.1 Effects of Deficiency of Transition Metals in the Brain

Iron deficiency is the most common and widespread nutritional deficiency in the world, affecting over 30% of the world's population (WHO, 2012). Iron deficiency results in malformation of red blood cells, growth impairment, reduced immune function, and deficits in cognition (Beard et al., 1993). Iron dyshomeostasis has been associated with cognitive dysfunction, neurological and neurodegenerative diseases (Burhans et al., 2005).

Manganese deficiency has only been observed in laboratory animals since the trace metal is abundant in human diets. Manganese deficiency results in impaired growth, skeletal defects, reduced reproductive function, birth defects, and abnormal lipid and carbohydrate metabolism (Aschner et al., 2005). Reduced manganese levels are seen in patients with osteoporosis and epilepsy, where manganese dyshomeostasis is associated with seizure susceptibility.

Copper deficiency is also rare, but symptoms include anemia, white blood cell abnormalities and losses, and osteoporosis (Fujita, Itakura, Takagi, & Okaga, 1989). Acquired copper deficiency in adults leads to neurodegeneration (Madsen & Gitlin, 2007). Iron transport is disrupted during severe copper deficiency with iron accumulation occurring in many tissues (Arredondo & Nunez, 2005).

1.2.2 Effects of Overload/Toxicity of Transition Metals in the Brain

Iron overload in the brain resulting from iron dyshomeostasis leads to saturation of iron transport and storage proteins, increased free iron in the cell, production of damaging free radicals, oxidative cellular damage,

followed by cell death (Beard et al.,1993). In the aging brain, iron levels and ferritin expression for intracellular iron storage increase. Under acidic conditions, however, iron can be released from ferritin and cause oxidative damage in the brain (Gaasch, Lockman, Geldenhuys, Allen, & Van der Schyf, 2007). Interestingly, some genetic iron metabolism disorders, such as hematochromatosis, do not necessarily result in iron overload in the brain (Gaasch et al., 2007) highlighting the brain's ability to maintain homeostasis in the face of systemic overload.

Manganese toxicity has been well characterized in cases of occupational overexposure to airborne manganese of miners, metallurgy workers and industrial workers (Pal, Samii, & Calne , 1999). Manganese neurotoxicity results in a psychiatric disorder resembling schizophrenia, followed by neurological disorder termed manganism with clinical symptoms closely resembling Parkinson's disease. Manganese overload primarily affects the basal ganglia in humans resulting in neuron damage and lesion formation in these gray-matter structures (Canavan, Cobb, & Drinker, 1934). The primary exposure route is inhalation (Roels et al., 1987), although manganese overload from drinking contaminated well water has also been reported and results in cognitive impairments (Sahni et al., 2007).

Copper does not accumulate in the body in the absence of a metabolic copper disorder; however, its homeostasis is disrupted in two genetic disorders: Menkes and Wilsons diseases (Madsen & Gitlin, 2007). Menkes disease is an X-linked disorder where the gene encoding the copper transport protein MNK is mutated. The loss of function mutation results severely reduced copper transport to the developing brain, resulting in widespread demyelination and neurodegeneration (Madsen & Gitlin, 2007). Wilson's disease is an autosomal recessive disorder with a loss-of-function mutation in the WND gene. Copper transport in the liver is impaired which leads to copper accumulation, copper-mediated damage, and cell death of hepatocytes. Copper then leaks into the plasma and accumulates in other tissues. Copper toxicity in the brain in Wilson's disease shares clinical symptoms with Parkinson's disease and other psychiatric symptoms of depression, cognitive defects, personality changes, psychosis, and schizophrenia (Madsen & Gitlin, 2007).

1.2.3 Interdependence of Transition Metal Levels in the Brain

The homeostasis of transition metals, such as iron, copper, and manganese in the brain is highly interdependent, and it is a mistake to consider specific transition metals in disease in isolation, although this is commonly done in studies.

Dietary or environmental changes in one or more of these metals can result in disrupted transport and distribution of transition metals, as well as metal transporter protein expression, in the brain (Erikson, Syversen, Steinnes, & Aschner, 2004; Garcia, Gellein, Syversen, & Aschner, 2006; Wang, Li, & Zheng, 2008). This is not surprising as iron, copper, and manganese metals share biological transport proteins due to their chemical and structural similarity (Fitsanakis, Zhang, Garcia, & Aschner, 2010). As an example, DMT-1 is largely involved in transport of both manganese and iron into the brain, and copper to a lesser extent (Garrick, et al., 2003; Gunshin, et al., 1997). In studies of rodent models with mutations in transport proteins it was found that both iron and manganese levels were disrupted with mutations in DMT-1 (Chua & Morgan, 1996; Fleming et al., 1997). Furthermore, in a dietary study where brain metal levels and transport protein expression were investigated in developing rats exposed to a high manganese diet via maternal milk during lactation, the brain manganese metal levels were increased, while iron levels decreased (Garcia et al., 2006). Concurrent with altered brain metal levels, there was also enhanced expression of DMT-1 and TfR proteins in the brain (Garcia et al., 2006). Studies such as these show that the regulation of transition metal levels in the rodent brain is interdependent and that homeostasis of multiple metals may be disrupted after overload or deficiency of one or more metals.

The research work in this thesis consists of two experiments where metal homeostasis may be disrupted in the brains of mice: *1.* following manganese injections typically administered in manganese-enhanced MRI (MEMRI) animal studies and *2.* following copper deficiency in a cuprizone model of demyelination. Instead of just focusing on the obvious metal changes (manganese in manganism and copper in the cuprizone model), we concurrently survey iron, manganese, and copper levels.

Chapter 2 – Methodology

The two studies of rodent models of metal-related brain disease in this thesis shared a common methodology. First, brain tissue samples were harvested from control and treated animals in each study and prepared for transition metal content measurements. These experiments were approved by the Animal Research Ethics Board at McMaster University. Second, the resulting small samples were measured for iron and copper concentration using x-ray fluorescence (XRF) and manganese concentration using neutron activation analysis (NAA). The two different techniques were needed for the metal measurements since the XRF spectra did not contain a manganese peak. The XRF system used in this work is not able to detect manganese in the tissue samples due to the low quantities of manganese in mouse tissues, as well as the energy of the manganese K-absorption edge, 6.54 keV being much lower than the incident x-ray photon energy, 17.5 keV, decreasing the probability of photoelectric absorption followed by manganese characteristic x-ray emissions. NAA is a more sensitive technique for manganese measurements owing to the large neutron capture cross-section of ^{55}Mn which allows for concentrations less than 1 μg/g of manganese to be detected and measured. The methodology is described in greater detail below.

2.1 Animal Work

2.1.1 Mice

Experiments were carried out in C57Bl/6 mice due to the availability of many disease and transgenic mouse models in this mouse strain, which expands the possibilities for future studies. Two groups of mice were studied in each experiment: healthy controls and a group treated to alter transition metal levels in the brain. The mouse brains were harvested following treatment and dissected to obtain individual regions. It is important to analyze transition metal levels regionally, since different brain regions can have widely different tissue properties and functions. The regions we investigate are those that can be accurately identified from gross anatomy and dissected in the mouse brain – the cerebellum, cortex, hippocampus, striatum, thalamus, and corpus callosum.

2.1.2 Tissue Harvest

Our experiments required fresh brain tissue to be harvested from mice, because fixation can affect metal levels in samples (Schrag, et al., 2010). The fresh brains were also quickly frozen and then processed to prevent possible diffusion of transition metals between regions. We harvested tissue from visceral organs to investigate systemic metal levels.

Mice were transferred individually from the cage to an induction chamber. Each mouse was induced in 100% oxygen at 5% isofluorane to reach surgical level anesthesia. The mouse was transferred to a nose cone and deep surgical anesthesia was confirmed by the absence of paw pinch reflex. The chest cavity of the mouse was then opened and approximately 2 mL of blood was drawn from the left ventricle by cardiac puncture, thereby sacrificing the animal. One kidney and a liver lobe were obtained and all tissue samples were stored on ice for the remainder of the procedure. The animal was decapitated with surgical scissors and the brain was harvested intact. The brain was immediately snap-frozen in isopentane in a liquid nitrogen bath to prevent diffusion of metal ions throughout the tissue prior to dissection. Blood, kidney, and liver samples and whole brains were transferred on ice to a freezer and stored at -80ºC until dissection and sample preparation.

2.1.3. Brain Dissection

The whole brain was partially thawed prior to dissection. Dissection was performed on an ice block to prevent complete thawing of the tissue. A dissection microscope was used to better view the brain structure boundaries and improve the dissection technique. An initial cut was made at the junction of the cerebellum and the cortex using a small surgical scalpel. The entire cerebellum was collected. The brain was then cut bilaterally at the longitudinal fissure separating the left and right hemispheres. At the posterior end of each hemisphere, the cortex was separated exposing the entire hippocampus, which was collected using a microspatula. The medial portion of the thalamus was then separated and collected. Next, the cortex was separated at the anterior part of the hemisphere exposing the entire striatum for collection. Lastly, the cortex

was separated from the attached white matter and its frontal region was collected.

Another whole brain was needed to dissect the white matter from the corpus callosum as this procedure destroys the brain for further dissection. The cerebellum was removed and the brain was cut bilaterally as described above. The cortex on each hemisphere was separated from the other brain structures with the attached white matter of the corpus callosum. The white matter was then carefully separated from the cortical grey matter using a microspatula.

2.1.4 XRF Sample Preparation

XRF tissue samples were prepared immediately following brain dissection. The XRF sample holder is a disc approximately 2 mm thick and 4 mm in diameter – usually, the entire tissue sample from each region is needed to fill this space. Smaller tissue samples from the harvested kidneys and livers were cut to fill the XRF sample holder. For blood, a small volume was drawn with a syringe and the XRF sample holder was filled with it. Care was taken not to have air bubbles in the blood sample. Fresh tissue was mounted onto XRF sample holders, covered with XRF thin film and secured with a small rubber “O” ring. The wet weight of the XRF sample was recorded. Excess XRF thin film was cut around the “O” ring and the sample was sealed in a small zipper storage bag. All XRF samples were kept frozen at -80ºC until measurement.

2.1.5 NAA Sample Preparation

NAA samples were prepared from the XRF samples following measurement since the analysis was done on the same brain tissue to decrease the number of mice sacrificed and dissections performed in the experiments. The brain tissue was transferred from the XRF sample holder into the NAA sample holder using a microspatula. New kidney, liver and blood NAA samples were made from unused tissue. The wet weight of the NAA samples was recorded. The samples were kept on ice until the freeze-drying procedure.

The NAA samples were freeze-dried to dehydrate the tissue samples to prevent water evaporation and pressure build-up in the NAA vial during irradiation which can lead to rupturing of the vial and radiation

contamination. During freeze-drying the tissue is first frozen and then the pressure in the freeze-drying chamber is reduced to remove water through sublimation. The brain, kidney, liver, and blood NAA samples were freeze-dried and sealed in small polyethylene NAA vials.

2.2 X-ray Fluorescence Spectroscopy

Energy-dispersive XRF spectroscopy was used to measure iron and copper in tissue samples. X-ray fluorescence is well-suited for the metal measurements in biological tissue samples in this research, since samples can be solids, such as organ tissue, or liquids, such as blood. As well, XRF is a non-destructive technique and samples can be sent for other analyses, such as histology, following XRF measurement if needed. In addition, XRF spectroscopy can identify and quantify both iron and copper in the same sample. This is possible since the energy of the photons detected using XRF is characteristic of the emitting element and the intensity is proportional to the elemental concentration.

In the XRF system used in this work, the sample was irradiated with ionizing x-rays. When an x-ray photon interacts with an atom in the tissue, it can be absorbed, scattered, or transmitted through the sample. These processes are discussed in the next section.

2.2.1 Interactions of X-rays with Matter

2.2.1.1 Photoelectric Absorption

In the photoelectric absorption process a photon is completely absorbed by the target atom, and a photoelectron is ejected from one of the bound shells of the atom (K, L, M, etc) (Fig.1). The energy of the incident photon must be at least equal to the binding energy of the photoelectron for photoelectric absorption to occur. When the incident photon energy is just above the binding energy of an electron the photoelectric interaction is most probable, and interaction probability decreases with increasing photon energy thereafter. The energy of the ejected photoelectron $\mathrm{E_e}$ is given by

$$\mathrm{E_e} = \mathrm{E_\gamma} - \mathrm{E_b}$$

where E_γ is the incident photon energy and E_b is the binding energy of the photoelectron.

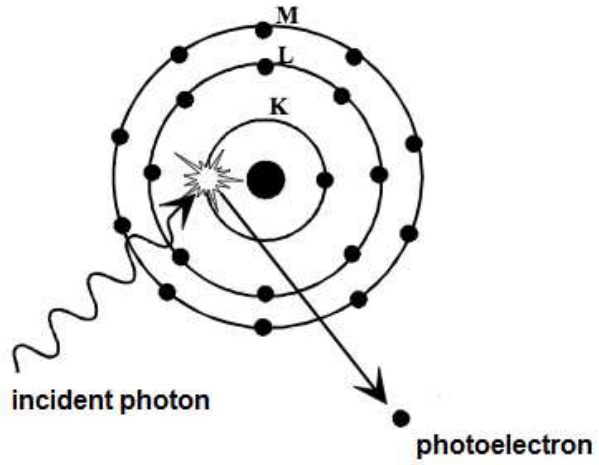

Figure 1. Photoelectric absorption process (modified from Heggie et al., 2001)

The photoelectric absorption process leaves an ionized atom with a vacancy in one of the shells. This vacancy is quickly filled by capture of an electron from an outer orbit of the atom. The atom then de-excites by emission of a characteristic x-ray or an Auger electron.

2.2.1.2 Characteristic X-rays

The energy released following electron transition from an outer orbit may appear as an x-ray whose energy is equal to the difference in the binding energies of the two electron states. An x-ray produced by an electron from the L shell filling a vacancy in the K shell is denoted as K_α (Fig. 2). The energy of the K_α x-ray photon is equal to the difference in the binding energies of the K and L shells. A K_β x-ray is emitted with the transition of an electron from the M shell to the K shell. The K, L, M, N,… designation of characteristic x-rays denotes which shell the x-ray originates from; and α, β , γ is used to label the x-ray that resulted from transitions of electrons from higher shells. Since a stable atom has discrete electron energy levels, the fluorescent x-ray emissions are characteristic of that atom. This is the basis of elemental analysis by energy-dispersive x-ray fluorescence.

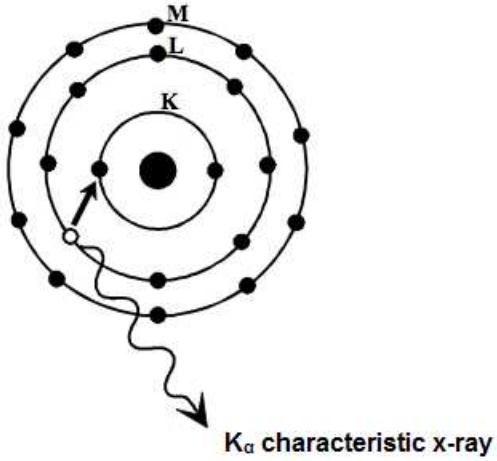

Figure 2. K_α characteristic x-ray emission following photoelectric absorption (modified from Heggie et al., 2001)

2.2.1.3 Auger Electrons

An atom may return to a stable state following the photoelectric absorption process by transferring the excitation energy directly to an outer shell electron. This electron is ejected from its orbital and is termed an Auger electron (Fig. 3). The energy of the Auger electron equals the difference between the atomic excitation energy (initial electron transition) and the binding energy of the orbit from which the Auger electron is ejected. The Auger effect is more probable in the elements with low atomic number, Z, than in the high Z elements.

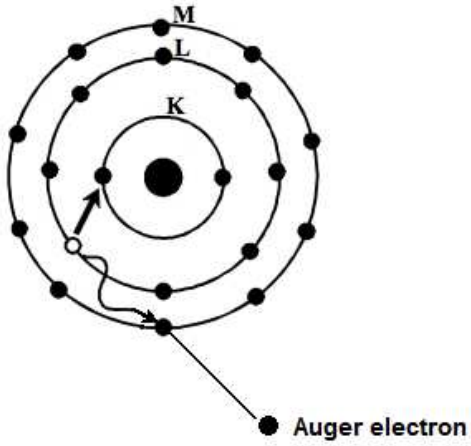

Figure 3. Auger electron emission following photoelectric absorption (modified from Heggie et al., 2001)

2.2.1.4 Fluorescence Yield

As described above not all of the incident x-ray photons result in fluorescent x-ray emissions by atoms and the fraction of all cases when characteristic x-rays are emitted is expressed by the fluorescence yield. A higher fluorescence yield for an element is desirable for XRF measurements.

The emissions of a characteristic x-ray or an Auger electron are competing mechanisms for atomic de-excitation in the photoelectric absorption process. The fraction of characteristic x-rays emitted following electron shell ionization of an element is given by the fluorescence yield. For K shell ionization, the fluorescence yield ω_K is given by

$$\omega_K = \frac{n_K}{N_K}$$

where n_K is the number of K_α X-rays emitted from the sample and N_K is the number of vacancies created in the K shell. The K-shell fluorescence yield is low for light elements and increases sharply with higher Z number as the fraction of Auger electrons (1-ω) decreases (Fig. 4).

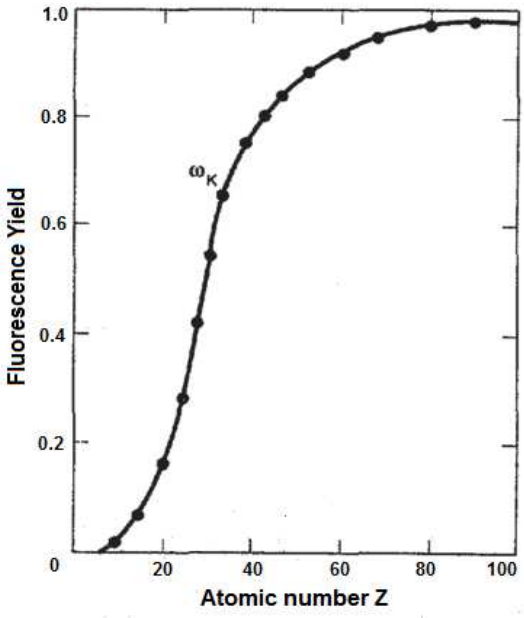

Figure 4. Fluorescence yield versus atomic number for K-shell ionizations (modified from Miller, 1991)

An ideal fluorescent yield for measurement with XRF would be 1. Measurement of iron with Z=26 and a K fluorescence yield of 0.31, and copper with Z= 29 and a K fluorescence yield of 0.41 (Roos, 1957) is still possible with this technique since enough atoms de-excite by emission of characteristic x-rays for adequate counting statistics during measurement.

2.2.1.5 Coherent Scattering

In an ideal measurement case, every photon interaction would occur via the photoelectric effect. However, there are a number of other mechanisms that compete with this interaction and should be considered.

In coherent scattering or Rayleigh scattering, the photon is scattered by the whole atom whereby it only changes direction. The scattered photon has the same energy as the incident photon and the target atom is left neither in an excited nor ionized state (Fig. 5).

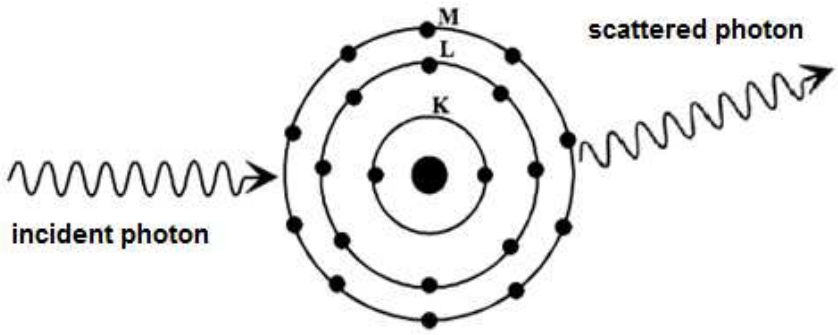

Figure 5. Coherent scattering (modified from Heggie et al., 2001)

The probability of coherent scattering is high for interactions with low energy photons and in elements with high Z number. The average scattering angle decreases with increasing photon energies.

2.2.1.6 Compton Scattering

In Compton scattering, also known as incoherent scattering, the incident photon interacts with an electron of a target atom. In the interaction, the incoming photon transfers some of its energy to the electron and is deflected through an angle θ. The scattered photon's energy is reduced and a recoil electron is ejected (Fig. 6).

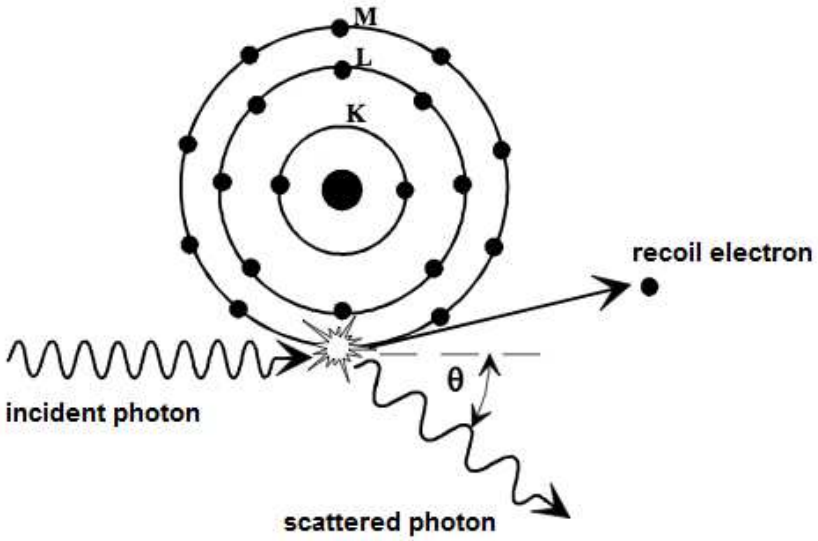

Figure 6. Compton scattering (modified from Heggie et al., 2001)

The kinetic energy of the recoil electron $\mathrm{KE_e}$ is given by

$$\mathrm{KE_e} = \mathrm{E_\gamma} - \mathrm{E_{\gamma'}},$$

where $\mathrm{E_\gamma}$ is the incident photon energy, $\mathrm{E_{\gamma'}}$ is the scattered photon energy; and the relationship between the incident and scattered photon energies is given by

$$\mathrm{E_{\gamma'}} = \frac{\mathrm{E_\gamma}}{1 + \frac{\mathrm{E_\gamma}}{\mathrm{m_e c^2}}(1 - \cos\theta)}$$

where $\mathrm{m_e c^2}$ is the electron rest-mass energy. The photon retains most of its energy at $\theta = 0°$ while maximum energy is transferred to the recoil electron at $\theta = 180°$; however, the incident photon always carries away some of its energy.

The cross-section of Compton scattering per atom of the tissue increases linearly as the Z number increases since it depends on the number of electrons in an atom for scatter.

2.2.1.7 Photon Transmission

The fraction of photons F that interact with atomic electrons in a sample is given by

$$F = 1 - e^{-\mu\rho x}$$

where μ is the mass attenuation coefficient, ρ is the sample density, and x is the sample thickness. The mass attenuation coefficient corresponds to the total cross-section or probability of all possible photon interactions in a unit mass. A plot of the mass attenuation coefficient versus photon energy for an element displays sharp discontinuities which are termed absorption edges (Fig.7). An absorption edge represents a sharp decrease in the photoelectric cross section for incident photon energies that are slightly lower than the binding energy of that electron state.

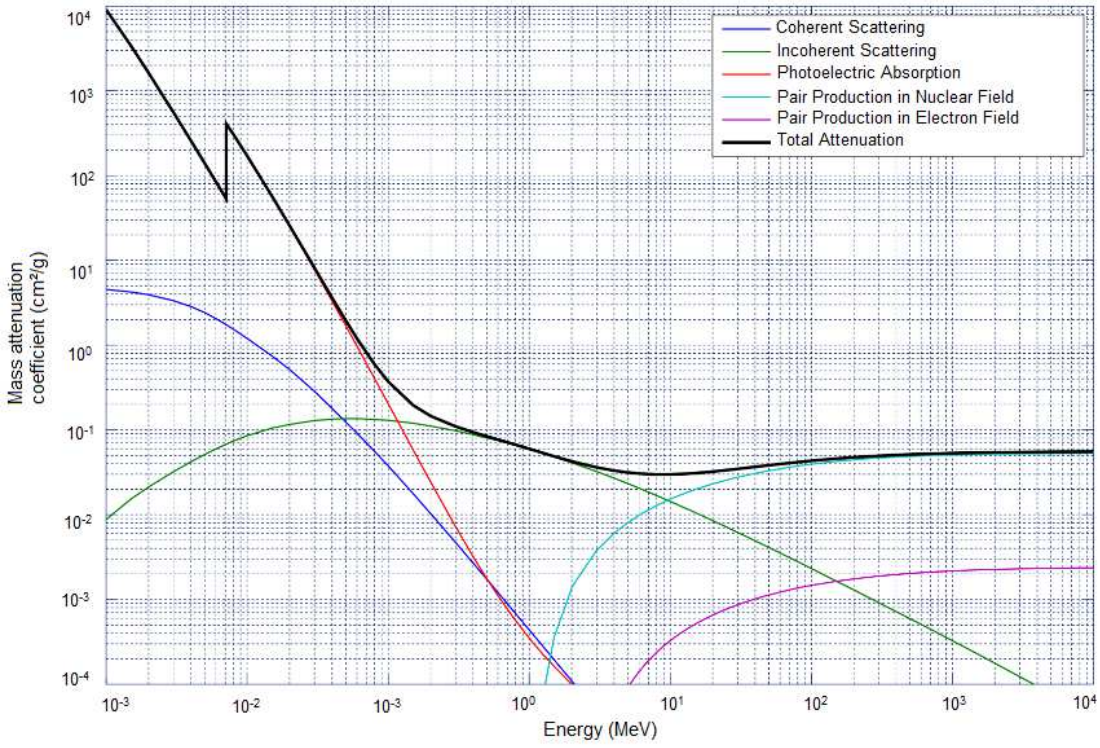

Figure 7. Mass attenuation coefficient as a function of energy for iron (modified from Jarekt, 2007)

At low energies the cross sections for coherent and Compton scattering are much smaller than the cross section for photoelectric absorption for an element given the energy is at least above the K-edge. For example, at 15 keV in iron the cross section for coherent scattering is 75 barns, 16.35 barns for Compton scattering and 5380 barns for photoelectric absorption (K, L, and M shells); and at 15 keV in copper the cross sections are 96 barns for coherent scattering, 18.24 barns for Compton scattering and 8000 barns for photoelectric absorption (Grodstein, 1957). Therefore, at the energy used in this research work (17.5 keV) the dominant photon interaction for elements of interest is photoelectric absorption.

2.2.2 X-Ray Fluorescence System

The instrumentation used in energy-dispersive XRF analysis consists of an excitation source to irradiate the sample; a detector to collect the fluorescence x-rays; a data analyzer system to sort the signals based on energy; and associated electronics. The irradiation source used in this research was an x-ray tube with a molybdenum target. The molybdenum target was specifically chosen to have an x-ray photon energy of 17.5 keV in order to maximize the number of photoelectric absorption events occurring in the irradiated tissue sample. As previously described, the photoelectric cross section for an electron is maximum at the absorption edge, just above the binding energy of that electron. A 17.5 keV x-ray beam allows for fluorescence measurements of a wide range of biologically relevant elements, including iron with a K-absorption edge at 7.11 keV and copper with a K-absorption edge at 8.98 keV. The radiation detector collecting fluorescence x-rays was a silicon drift detector (SDD). The SDD is suitable for XRF analysis which deals with high count rates and requires high energy resolution, since the entire thickness of the detector is sensitive to radiation, which allows it to record high photon numbers and the output capacitance of the detector is very low, which prevents electronic noise detection (Lechner et al., 2004). The fluorescence photons detected from the sample are organized into a histogram of number of events versus pulse-height related to the energy of the detected event. The stored spectrum is then displayed and the data can be further analyzed.

2.2.3 Iron and Copper Measurements using XRF

X-ray fluorescence measurements were made on a custom-built X-ray fluorescence system and the measurement protocol used to quantify the iron and copper content in the regional brain, kidney, liver and blood tissue specimens is described below.

The x-ray source was a molybdenum target tube. The output beam was monochromated to approximately 17.5 keV and focused on a sample size of 2 by 2 mm using multi- layer optics. Samples were mounted at 45° between the incident x-ray beam and the XFlash LE SDD Detector (Bruker AXS GmbH, Karlsruhe, Germany), which were oriented at 90 degrees to each other, and located 5 mm away from the XRF detector during data collection. Measurements were made with the x-ray tube operating at 50 kV and 500 mA with a counting time of 26100 seconds (7.25 hours), or at 50 kV and 320 mA with a counting time of 52200 sec (14.5 hours) to have approximately the same x-ray beam intensity during the day and overnight measurements. Long measurement times were required to obtain good counting statistics due to the low concentrations of iron and copper in the rodent brain. The elements of interest, iron and copper, were identified by the photopeaks associated with their K_{α} fluorescence photon emission at 6.4 keV and 8.04 keV respectively.

XRF spectra were analyzed using PeakFit spectrometry analysis software (PeakFitTM SPSS Inc., AISN Software Inc.). The fluorescence photopeaks were smoothed and the background was subtracted. A Gaussian function was used to fit the photopeaks and the net area of the peak was determined. The same procedure was applied to analyse the escape Si peak, tail, Compton, and Coherent scatter peaks of every spectrum. The ratio of fluorescence to scatter peak areas was taken where the total scatter peak area was used as a normalization factor for the detected fluorescence photons to account for differences in each measurement such as different measurement times or different x-ray flux. The ratio of fluorescence to scatter peak areas was then used to calculate the elemental concentrations from standard calibration curves.

Calibration curves were constructed for each element. Calibration solutions with known concentrations of the elements (0-64.2 ppm iron and 0-52.8 ppm copper) were measured using the same procedure as the

brain tissue samples. A linear relationship between the elemental quantity and ratio of fluorescence to scatter photopeak areas over the relevant concentration range was established. The linear calibration equations were used to quantify the iron and copper concentrations in the six brain regions and organs.

The accuracy of the XRF method for quantification of iron and copper in brain, kidney, liver, and blood tissues was validated using a standard reference material of the same weight as the samples. This material was homogenized lobster (LUTS-1, “Non defatted lobster hepatopancreas reference material for trace elements,” National Research Council, Canada) due to its material matrix of mainly water and lipid, similar to brain tissue. The certified and experimentally obtained concentrations of copper and iron in the LUTS-1 reference material are given below in Table 1.

Element	Certified value (mg/kg)	Experimental value (mg/kg)
Cu	15.9±1.2	17.4±1.4
Fe	11.6±0.9	12.4±2.5

Table 1. Certified and experimental concentrations of Cu and Fe in the LUTS-1, “Non defatted lobster hepatopancreas reference material for trace elements,” National Research Council, Canada.

The validation using the LUTS-1 reference material shows that the XRF method is accurate for the measurements of iron and copper in tissue samples of similar size and composition to our mouse tissue samples.

2.3 Neutron Activation Analysis

NAA was used to measure manganese concentrations in tissue samples. NAA is a well-suited technique for manganese metal measurement in this research work, since it is a non-destructive technique with detection sensitivity for manganese of less than 1 μg (Pidruczny, Butler, Ernst, Collins, & Avelar, 1994). As well, sample preparation is not extensive and NAA samples can be solids or liquids.

2.3.1 Principles of Neutron Activation Analysis

NAA is a nuclear technique based on the reaction between neutrons and target nuclei. When a sample is irradiated by a flux of neutrons, stable nuclides undergo neutron capture reactions to produce radionuclides. The neutron capture reaction is given by

$$^{A}\mathrm{Z}(\mathrm{n},\gamma)^{A+1}\mathrm{Z}$$

where n is a neutron, γ is a gamma photon, and A is the atomic mass.

The radioactive nuclides in the activated sample then decay by emission of prompt and delayed gamma photons and beta particles according to a characteristic half-life. Knowledge of the half-life and gamma photon energy of a given radionuclide can identify the corresponding element in a sample.

The radioactive emissions from the activated sample are measured using gamma spectroscopy. In prompt gamma neutron activation analysis, the gamma rays emitted with extremely short half-lives on the order of milliseconds are measured during irradiation. Following irradiation the delayed gamma rays with longer half-lives are measured, which is the technique used in this research work. Qualitative analysis involves identifying the elemental composition of the sample since the energy of the emitted gamma photons is characteristic of a radionuclide. Quantitative analysis measures the intensity of the characteristic gamma-ray lines in the spectrum obtained from the irradiated sample. In comparative instrumental NAA the quantitative analysis is standardized relative to a known quantity of an elemental standard. This relative approach simplifies data analysis as it reduces the experimental parameters that must be accounted for and is the technique used in this research.

2.3.2 Irradiation Facilities

A neutron source is required for NAA, which can be a radioisotope, nuclear generator, or nuclear reactor. Nuclear reactors are the most efficient neutron sources for elemental analysis due to the high neutron flux. Neutrons in the thermal energy range are typically chosen since the majority of elements have a high neutron capture cross-section, which

gives a measure of the probability of neutron capture, in the thermal region (Mughabghab, 2003). For example, the thermal neutron capture cross-sections (averaged for different isotopes) of the metals of interest in this thesis are as follows: 13.36 ± 0.05 barns for manganese, 3.78 ± 0.02 barns for copper, and 2.56 ± 0.35 barns for iron (Mughabghab, 2003). In this work, the McMaster Nuclear Reactor (MNR) was used as the neutron source to irradiate the samples.

The MNR is a thermal, open-pool type research reactor facility which typically operates at a power of 2-3 MW. The reactor contains a number of irradiation sites, including the thermal RABBIT site adjacent to the core used for NAA in this research (Fig.8). The Centre for Neutron Activation Analysis (CNAA) is an on-site laboratory equipped for nuclear elemental analysis. The thermal RABBIT irradiation site is accessible from the CNAA via an automatic pneumatic transport system for remote sample delivery and retrieval. The neutron flux at this RABBIT site is 3×10^{12} $\mathrm{n/cm^2 s}$ (Pidruczny et al., 1994).

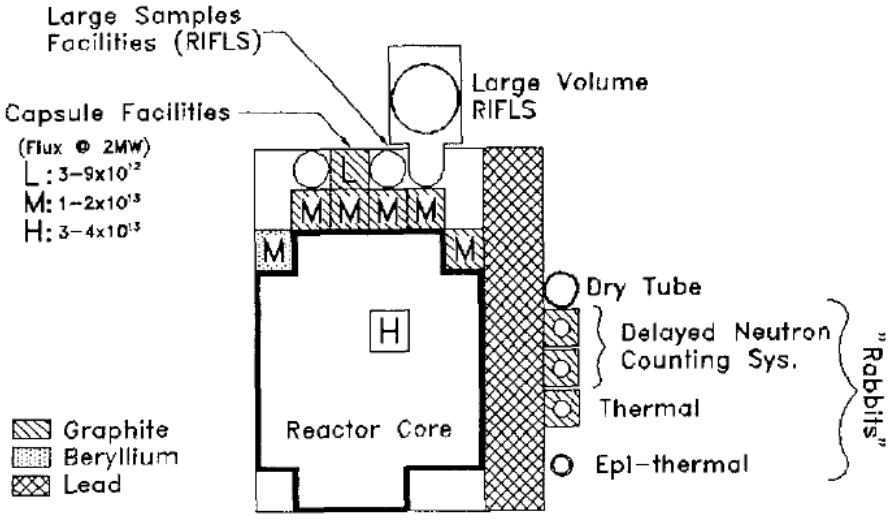

Figure 8. Location of irradiation sites at the McMaster Nuclear Reactor (Pidruczny et al., 1994).

2.3.3. Gamma Spectroscopy

The CNAA has several gamma measuring systems for spectroscopy analysis of the activated samples. The gamma spectroscopy equipment used for this work consists of a high-purity germanium (HPGe)

gamma detector; a PC based multichannel analyzer (MCA); associated electronics such as preamplifier, high voltage filter, shaping amplifier; and software for data analysis.

HPGe detectors are used in gamma spectroscopy due to their excellent energy resolution. In order to reduce electronic noise from a leakage current, HPGe detectors must be cooled to liquid nitrogen temperatures due to the small bandgap energy of germanium. The germanium crystal is encased in a cryostat under high vacuum with the preamplifier (Knoll, 2000). The HPGe detector used in this research is an n-type high-purity germanium coaxial closed-ended semiconductor crystal. It consists of an n-type cylindrical germanium crystal with the p^+ electrode at its outer surface and the n^+ electrode located at the inner surface of the central hole forming a p-n junction at the outer surface of the crystal. The depletion region is increased by reverse biasing the p-n junction. The electric field within the region of the junction allows for collection of the electron-hole pairs generated within the depletion region by interaction with gamma photons emitted by the radionuclides in the activated sample. The motion of electrons and holes drifting toward the collecting electrodes creates an electrical signal proportional to the initial deposited energy by the photon (Knoll, 2000).

The electrical signal is then processed in the preamplifier, high voltage filter and shaping amplifier, to produce a filtered, shaped and amplified signal pulse. The multichannel analyzer sorts the signals into a histogram of number of events versus pulse-height. Following an energy calibration, a spectrum of counts versus energy is displayed by the PC based MCA. The measured count of gamma rays of a specific energy depends on the quantity of the element in the biological sample. The count rate,R, of the detected gamma photons emitted by a radionuclide is related to the amount of the nuclide activated in the sample, $\mathrm{N_{sample}}$, by

$$\mathrm{R} = \varepsilon\,\gamma\,\mathrm{N_{sample}}\,\varphi\,\sigma(1-\mathrm{e}^{-\lambda \mathrm{t_i}})\mathrm{e}^{-\lambda \mathrm{t_d}}$$

where ε is the absolute detector efficiency, γ is the absolute gamma-ray abundance, φ is the neutron flux, σ is the neutron capture cross-section, λ is the decay constant, t_i is the irradiation time, t_d is the decay time.

In practice, it is difficult establish all of the above parameters and the comparative instrumental NAA method is used in this work. If a standard is irradiated and measured using the same protocol as the sample, then the quantities of the nuclide are related by

$$\frac{N_{sample}}{N_{standard}} = \frac{A_{sample}}{A_{standard}}$$

where A_{sample} is the peak area of a gamma ray of a specific energy in the sample, $A_{standard}$ is the peak area of a gamma ray of a specific energy in the standard, and $N_{standard}$ is the amount of nuclide activated in the standard.

2.3.4 Manganese Measurements using NAA

Comparative neutron activation analysis was used to measure the manganese content in the six different brain region tissues samples, and in the visceral organs using the measurement protocol described below, which was developed by a previous Masters' student in the lab. Standards of 1 µg manganese were made up from a 1000 µg/mL standard manganese stock solution (J.T. Baker 6458-04, NJ).

The manganese standards and mouse tissue specimens were irradiated for 1200 seconds using a thermalized RABBIT neutron irradiation site at the McMaster Nuclear Reactor. The half-life of the resulting manganese isotope ^{56}Mn is 9281 seconds (2.578 hours). After a 4500 second delay time, the irradiated samples were measured using an Aptec HPGe spectroscopy system with a counting time of 600 seconds. The HPGe detector is an Ortec model GMX-25195-S detector biased at 3 kV with a 0.5 mm beryllium window. The detector is cooled by a 16 L liquid nitrogen dewar in the Ortec CFG-SH-GMX configuration. The PC based MCA is an Aptec PCMCA/WIN V4.3 Release 6 system configured to 4096 channels.

The standards were measured as the first and last samples and averaged to account for temporal differences in neutron flux. The photopeak associated with the 847 keV gamma ray decay of ^{56}Mn was chosen for analysis since it has the highest emission probability. The area of the peak was determined using the Aptec software for the standards and tissue samples. The ratio of the specimen to averaged standard peak

areas was used to calculate the mass of manganese in the specimen. The manganese concentration in the six brain regions, liver, kidney, and blood samples was then obtained by dividing the mass of manganese in the sample by the wet weight of the sample.

The accuracy of the comparative NAA method for quantification of manganese in brain tissue, visceral organs, and blood was validated using United States' National Institute of Standards and Technology (NIST) certified bovine muscle powder (beef) standard (Reference Material 8414) containing a similar weight of Mn to our freeze-dried samples. The certified and experimentally obtained concentrations of manganese in the bovine muscle powder reference material are given below in Table 2.

Element	Certified value (μg/g)	Experimental value (μg/g)
Mn	0.37±0.09	0.39±0.09

Table 2. Certified and experimental concentrations of Mn in the bovine muscle powder (beef) standard (Reference Material 8414), National Institute of Standards and Technology, USA.

The validation using the bovine muscle powder reference material shows that the NAA method is accurate for the measurements of manganese in mouse brain tissue.

Chapter 3 – Manganese Experiment

3.1 Manganese-Enhanced Magnetic Resonance Imaging

3.1.1 Magnetic Resonance Imaging and Paramagnetic Metals

Magnetic resonance imaging (MRI) is an excellent tool in animal research since it is a non-invasive technique that provides high resolution and intrinsic soft-tissue contrast. The basic image contrast results from differences in two MRI parameters: the longitudinal and transverse relaxation times, T_1 and T_2 respectively, in different tissues. Paramagnetic ions with unpaired electrons increase the MR relaxation rates of tissue water protons, reducing T_1 and T_2 (Bloch, Hansen, & Packard, 1946; Bloembergen, Purcell, & Pound, 1948). Biologically significant metals, such as copper, iron, and manganese, contain unpaired electrons as divalent and trivalent ions, and hence alter the MRI signal of brain tissue. As a result paramagnetic ions can be used as contrast agents in MRI (Donnelly, Xiao, & Wedd, 2007), such as the use of divalent manganese to provide contrast in animal neuroimaging (Silva, Lee, Aoki, & Koretsky, 2004). The application of Mn^{2+} as a contrast agent is limited to animal studies due to its cellular toxicity. As previously described chronic manganese exposure in humans leads to a Parkinson's-like condition called manganism, while acute overexposure can cause hepatic failure (Chandra & Shukla, 1967) and cardiac toxicity (Wolf & Baum, 1983).

Manganese-enhanced MRI is widely used in animal brain imaging with three specific applications (Bock & Silva, 2007; Koretsky & Silva, 2004). Firstly, MEMRI has been used to trace neuronal connections in the rodent (Pautler, Silva, & Koretsky, 1998), avian (Van der Linden, Van Meir, Tindemans, Verhoye, & Balthazart, 2004), and primate brains (Yamada et al., 2008). Secondly, since divalent manganese (Mn^{2+}) can enter excitable cells via voltage-gated calcium channels, MEMRI has been applied to image active areas of the brain and heart (Aoki, Naruse, & Tanaka, 2004; Yu et al., 2011). Thirdly, systemically administered manganese provides better whole-brain contrast enhancing anatomical detail in MRI images (Silva et al., 2008; Watanabe, Frahm, & Michaelis, 2010). MEMRI studies typically use manganese for T_1 contrast on MRI images and to produce T_1

maps. Manganese accumulation has been quantitatively related to the shortened T_1 values which appear as a brightening of the image on T_1-weighted MRI (Bock, Kocharyan, & Silva, 2009; Chaki et al., 2000). In the case of manganese neurotoxicity in humans, most notably occupational manganese overexposure, signal hyper-intensities can be visualized in the basal ganglia on T_1-weighted MRI images which have been shown to relate to the dose of manganese overexposure (Kim et al., 1999; Kim, 2004; Shin et al., 2007)

3.1.2 MEMRI and Transition Metal Homeostasis

The application of MEMRI in animal studies assumes that MR relaxation rates are proportional to the effective manganese concentration in tissue (Afonso, Lee, Aoki, & Koretsky, 2004). This implies that the signal hyper-intensity on a T_1-weighted MR image is directly related to amount of manganese accumulated in the region of interest. However, given that manganese uses the same transporter proteins as other bio-metals, the contrast seen in MEMRI may be a result of disrupted metal homeostasis rather than manganese accumulation alone. It is possible that transition metal dyshomeostasis following manganese administration in MEMRI experiments may significantly affect the concentrations of copper and iron ions in tissue as well, which will alter the MR relaxation rates. Then, the changes in MRI signal in brain tissue will be related to changes in several paramagnetic metals, such as manganese, copper, and iron.

The effect of manganese exposure on transition metal levels in the brain has been mostly investigated in chronic low-dose manganese studies. When rats were injected with 3 mg/kg Mn weight/body weight manganese solution for four weeks, no significant changes in iron levels in any of the brain regions were observed; while, copper levels were found to increase in several brain regions examined (Sheuhammer & Cherian, 1981). In another study, at the same dose and a longer treatment regimen of fourteen weeks, iron concentrations in rat brain regions also did not change significantly between the control and manganese-treated groups (Zhang et al., 2009). In a developmental rat model of chronic manganese treatment with doses of 1, 10, or 20 mg Mn/ml of drinking water, iron and copper levels were found to increase in some brain regions (Lai, Minski, Chan, Leung, & Lim, 1999). These studies show that metal homeostasis in the rodent brain may be disrupted with low-dose chronic manganese

exposure. Furthermore, administration of acute high-doses of manganese may have a more severe effect in brain metal homeostasis and significantly disrupt metal levels. The typical doses used in MEMRI animal studies range from 30-180 mg/kg Mn weight/body weight manganese solution administered as a single or fractionated injections (Grunecker et al., 2010; Bock, Paiva, & Silva, 2008). The effects of manganese doses used in MEMRI on transition metal homeostasis have not been investigated extensively; although, one study did look at the effects of acute single-dose manganese exposure on trace metals in the rat brain. At single doses of 25, 50, and 100 mg $MnCl_2$/kg injected in rats, iron levels increased in many regions of the brain and copper levels were unchanged (Chen, Cheng, Lin, Chen , & Huang, 2006).

In the manganese study in this work, we investigated transition metal levels in the brains of mice following high-dose manganese injections typically used in MEMRI animal studies. A treatment regimen of fractionated injections of 30 mg $MnCl_2$/kg every twenty-four hours has been shown to produce excellent MEMRI contrast with minimal toxic side effects in C57Bl/6 mice (Grunecker et al., 2010). We looked at metal levels of manganese, iron, and copper in brain regions of mice treated with this dose of manganese for four days. X-ray fluorescence and neutron activation analysis techniques were used for metal measurements in excised brain and peripheral organ tissue.

3.2 Manganese Treatment

The manganese experiment was carried out in adult male C57Bl/6 mice obtained from Jackson Laboratories, ME at 16 weeks of age. Two groups of treated (n=5) and two groups of control (n=5) mice were needed to dissect the cerebellum, hippocampus, thalamus, striatum, cortex brain regions in one group, and the corpus callosum in another group. Mice were housed three to a cage on a 12 hour light/dark cycle and fed *ad libitum* 8640 Teklad 22/5 Rodent Diet (Harlan Laboratories Inc., WI). Animals were allowed to adjust to their surroundings for at least one week prior to use.

A treated group of mice (n=5) received intraperitoneal injections of 30 mg/kg $MnCl_2 \cdot 4H_2O$ dry chemical weight/body weight manganese solution in bicine buffer spaced 24 hours apart for four consecutive days.

The manganese solution was prepared by adding 500 mL of HPLC grade water to 4.18 g $MnCl_2 \cdot 4H_2O$ and 16.3 g bicine buffer, and titrating with NaOH to bring the solution to physiological pH. The concentration of manganese in the solution was 100 mM and the injected volume for each mouse was about 0.1 ml. Treated mice were monitored after the injections to observe general health during the course of the treatment. Measures included body weight, coat appearance, posture, behaviour and dehydration. A control group of mice (n=5) received no injections. Animals were sacrificed 24 hours following the final injection in the treated mice.

3.3 Manganese Statistical Analysis

Statistical analyses were performed using SPSS software (IBM SPSS Statistics Version 20.0, IBM Corp.). Data was first assessed for normality using the Shapiro-Wilk test of normality. Levene's test of equality of error variances was then used to test the homogeneity of variances of the metal concentrations across groups. A two-way ANOVA followed by a Tukey HSD post-hoc test were used to test the significant differences in metal concentration between the brain regions of control and manganese treated mice. The significant difference in manganese concentration in the blood was tested using an independent T-test, while the Mann-Whitney U test was used for the liver and kidney data. Significant differences in copper and iron concentrations in the blood, liver, and kidney data were tested using independent T-tests.

3.4 Manganese Experimental Results

General health status of the animals was assessed following manganese injections. No adverse health effects, such as rough hair coat, hunched posture, abnormal behaviour or dehydration were observed in the treated mice and there was no significant difference in animal weight after the injections ($p>0.05$). Mice began the study weighing 31±3 g (mean± standard deviation, n=10). The average weight in the treated group at the time of sacrifice was 30±2 g (n=5) and in the control mice it was 29±2 g (n=5).

The regional brain manganese concentrations in the control and manganese treated mice receiving fractionated manganese injections are

given in Figure 9, as measured with NAA. There was a significant accumulation of manganese in all of the brain regions at the p=0.05 level. The manganese concentration increased the most in the cerebellum and thalamus, with increases of 2.04 µg/g (metal weight to wet tissue weight) to 396% of the Mn concentration in the control cerebellum and 1.99 µg/g to 353% of the Mn concentration in the control cerebellum; while the cortex increased the least with an increase of 0.87 µg/g to 216% of the Mn concentration in the control cortex.

Inter-regional differences of manganese accumulation were significant between the treated cortex and cerebellum, thalamus ($p<0.05$).

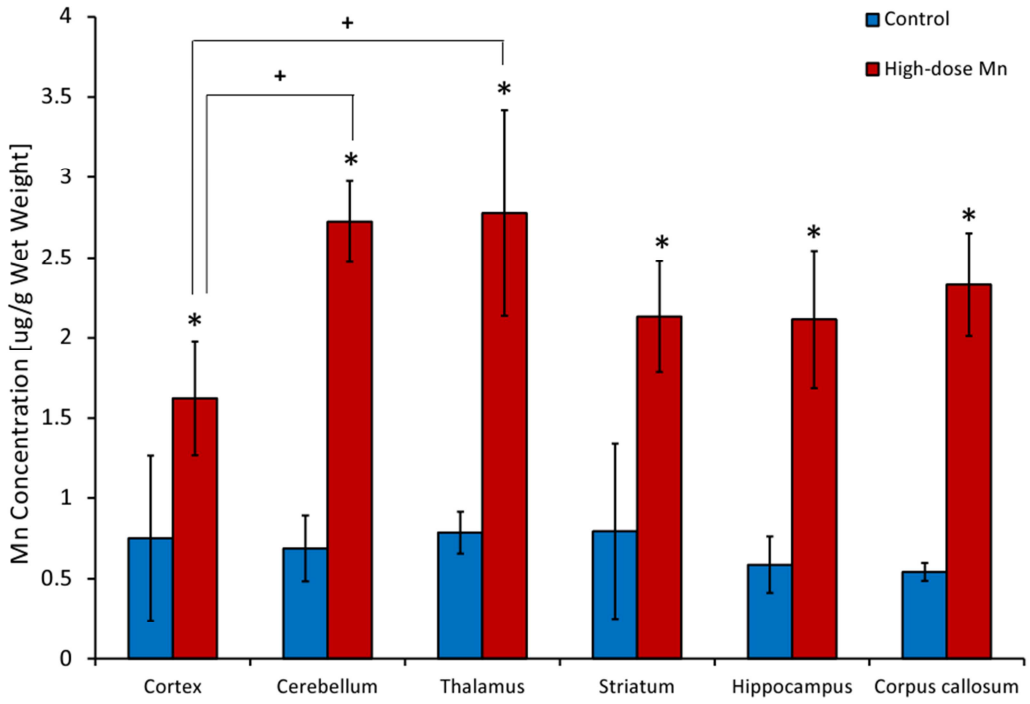

Figure 9. Manganese concentration (mean ± std. dev., n=5 for each group) in different brain regions of C57Bl/6 control mice and mice treated with a dose of 30 mg $MnCl_2\,4H_2O$/kg. Mn concentration was determined using comparative NAA. Statistical significance between control and treated groups at $p<0.05$ is denoted by the * symbol. Statistical significance between brain regions within the treated group at $p<0.05$ is denoted by the + symbol.

Iron concentrations as measured with XRF in the control and manganese treated mouse brain regions are shown in Figure 10. There

was a statistically significant decrease in the level of iron in the thalamus of the treated mice compared to control at the p=0.05 level. In that structure, iron was reduced by 6.82 μg/g to 70% of the Fe concentration in the control thalamus. There was no statistically significant difference in iron levels between the control and treated groups in the rest of the brain regions considered.

The iron concentration was significantly higher in the control thalamus than in the other five brain regions at the p=0.05 level. There was also a significant difference in iron concentration between the treated cortex and treated corpus callosum (p<0.05).

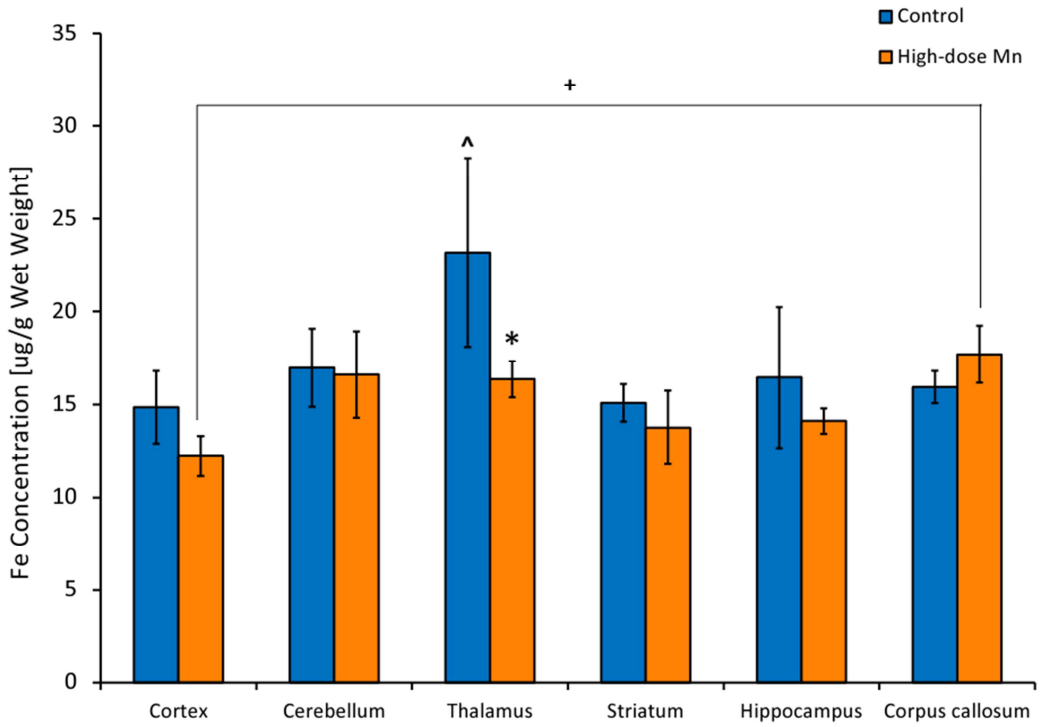

Figure 10. Iron concentration (mean ± std. dev., n=5 for each group) in different brain regions of C57Bl/6 control mice and mice treated with a dose of 30 mg $MnCl_2\,4H_2O$/kg. Fe concentration was determined using XRF. Statistical significance between control and treated groups at p<0.05 is denoted by the * symbol. Statistical significance between the five brain regions and the thalamus within the control group at p<0.05 is denoted by the ^ symbol. Statistical significance between brain regions within the treated group at p<0.05 is denoted by the + symbol.

Figure 11 shows the regional brain copper concentrations as measured with XRF in the control and manganese treated mice. There

was no significant change in the copper levels in the brains of mice treated with manganese compared to the control group.

Inter-regional differences in copper concentration measured with XRF were significant between the treated corpus callosum and cortex, hippocampus ($p<0.05$). There was also a significant difference in copper concentration between the control thalamus and striatum ($p<0.05$).

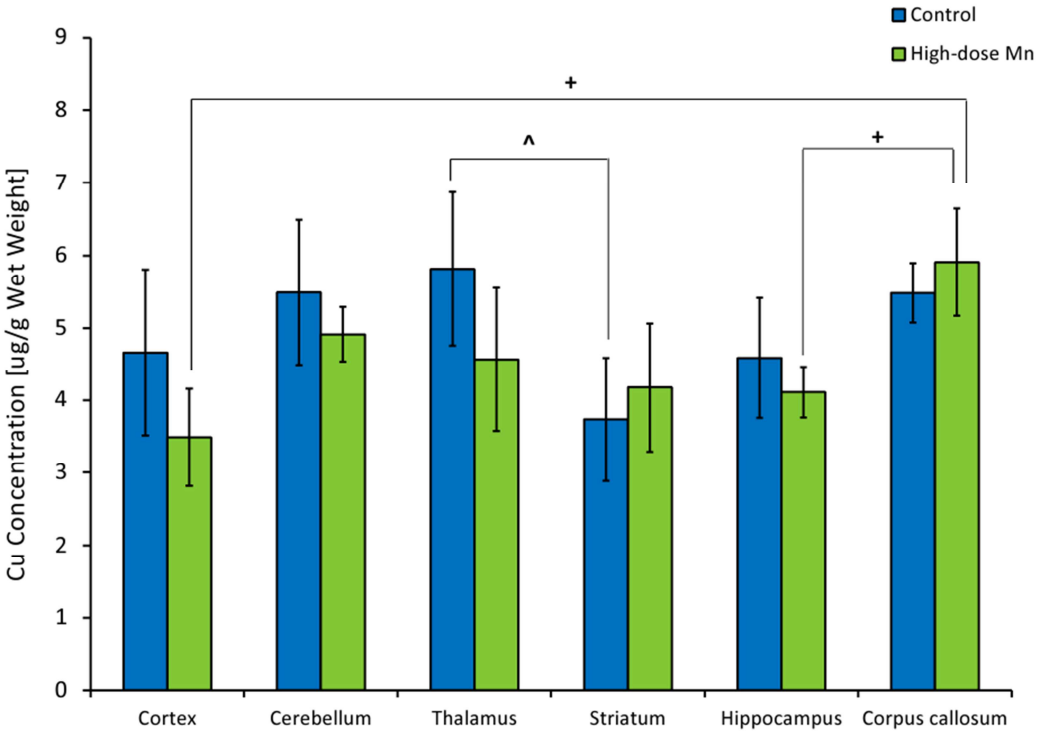

Figure 11. Copper concentration (mean ± std. dev., n=5 for each group) in different brain regions of C57Bl/6 control mice and mice treated with a dose of 30 mg $MnCl_2\,4H_2O$/kg. Cu concentration was determined using XRF. Statistical significance between brain regions within the control and treated groups at $p<0.05$ is denoted by the ^ and + symbol respectively.

The manganese, iron, and copper concentrations in the blood collected by cardiac puncture 24 hours following the last manganese injection at sacrifice are shown in Figure 12. The metal concentrations in the blood did not change significantly following manganese injections compared to control animals ($p>0.05$).

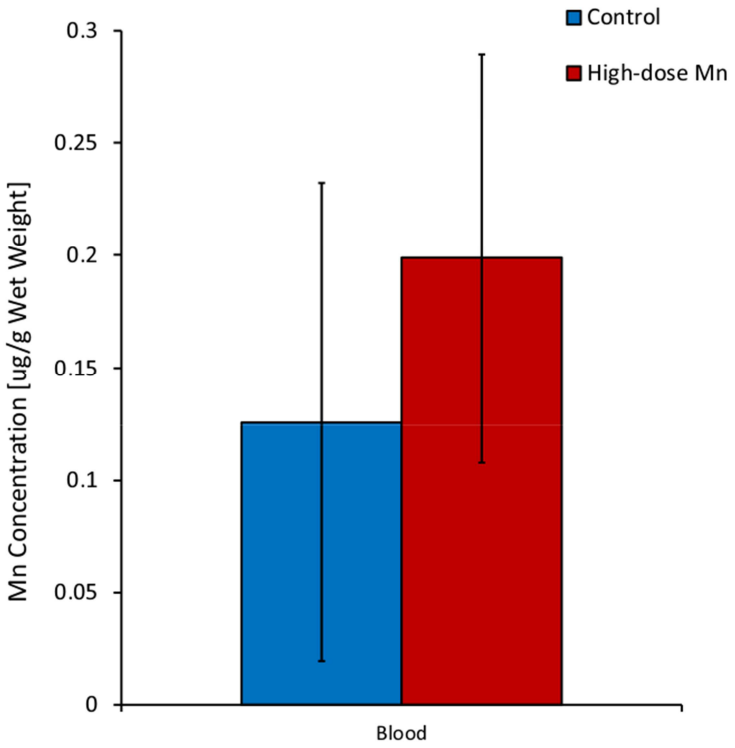
Control
High-dose Mn
Mn Concentration [ug/g Wet Weight]
0.3
0.25
0.2
0.15
0.1
0.05
0
Blood

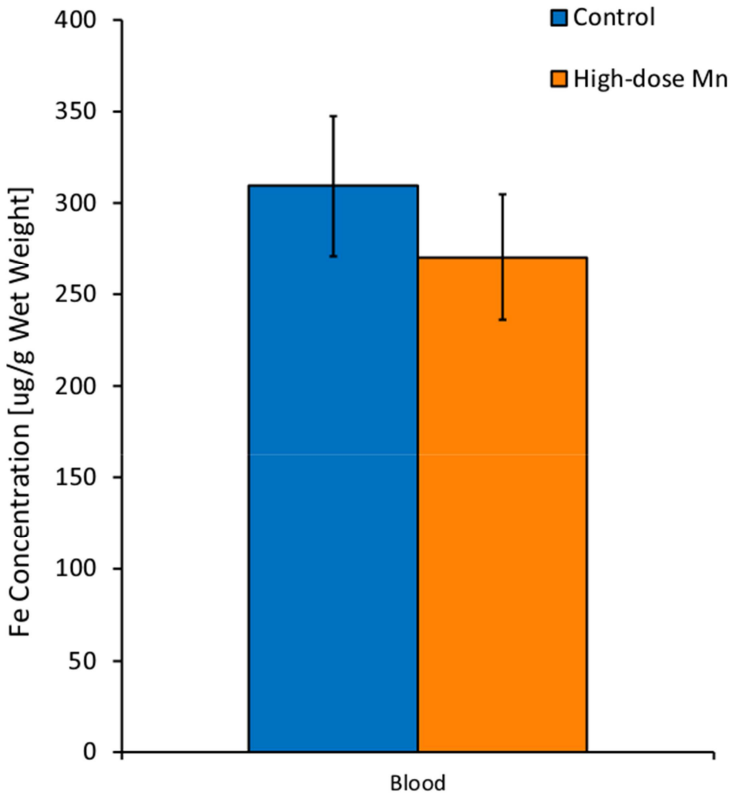
Control
High-dose Mn
Fe Concentration [ug/g Wet Weight]
400
350
300
250
200
150
100
50
0
Blood

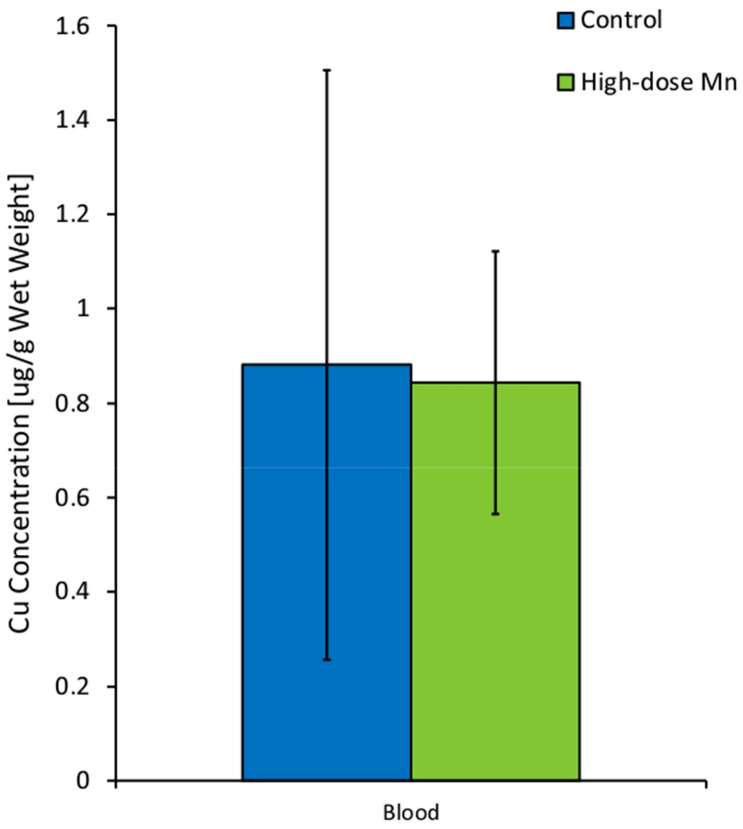

Figure 12. Manganese, iron, and copper concentrations (mean ± std. dev., n=5 for each group) in the blood of C57Bl/6 control mice and mice treated with a dose of 30 mg $MnCl_2\,4H_2O$/kg. Mn concentration was determined using comparative NAA. Fe and Cu concentrations were determined using XRF.

Figure 13 shows the manganese, iron, and copper levels in the visceral organs of manganese treated and control mice. There was a significant increase in manganese in both the liver and the kidney at the p=0.05 level. The manganese concentration in the treated liver increased by 1.59 µg/g to 245% of the Mn concentration in the control liver; while the treated kidney had a much larger increase of 17.9 µg/g to 1320% of the Mn concentration in the control kidney. There was no significant changes in the iron or copper concentrations in the liver and kidney in the treated mice (p>0.05).

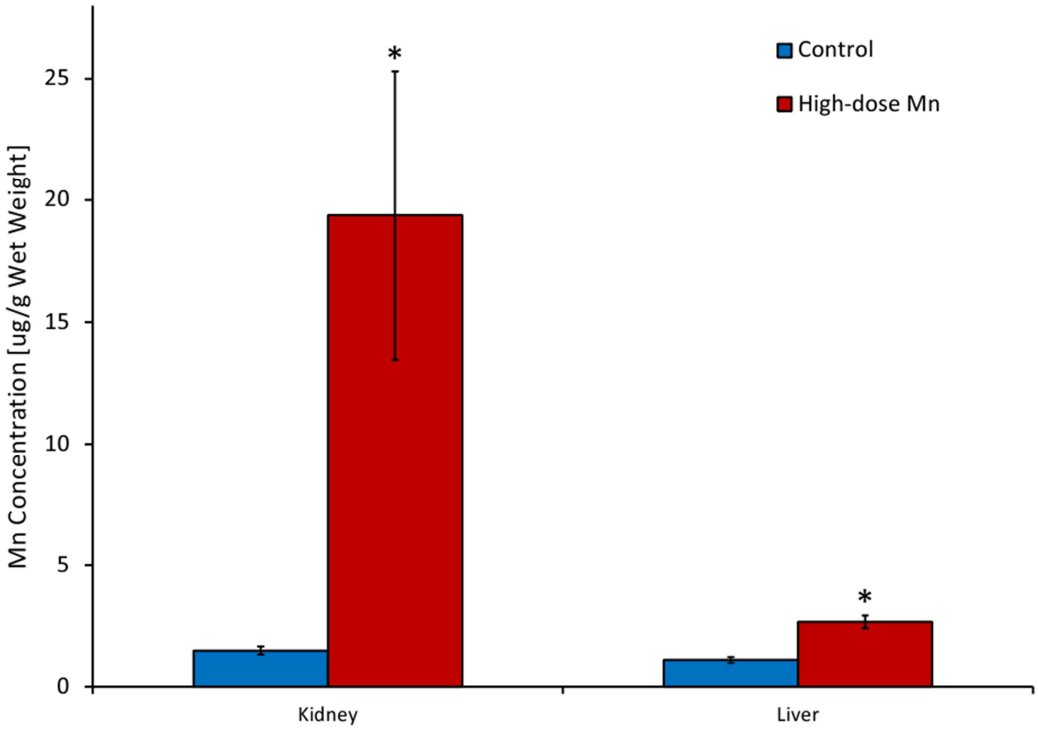
Control
High-dose Mn
Mn Concentration [ug/g Wet Weight]
25
20
15
10
5
0
*
*
Kidney
Liver

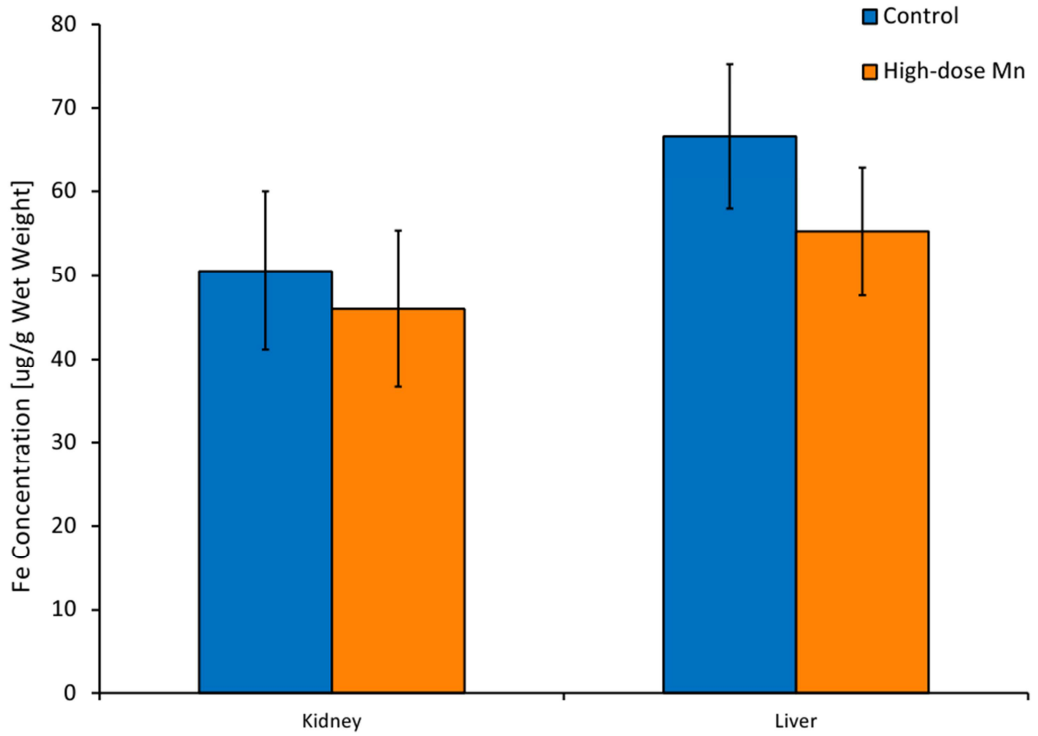
Control
High-dose Mn
Fe Concentration [ug/g Wet Weight]
80
70
60
50
40
30
20
10
0
Kidney
Liver

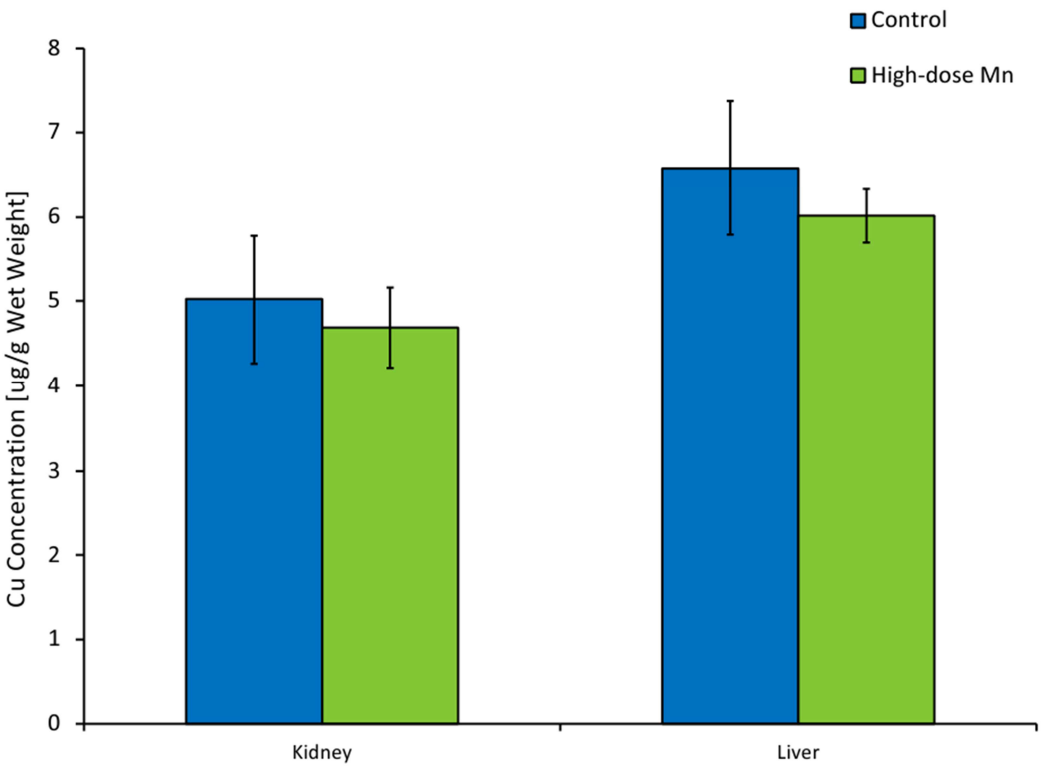

Figure 13. Manganese, iron, and copper concentrations (mean ± std. dev., n=5 for each group) in visceral organs of C57Bl/6 control mice and mice treated with a dose of 30 mg $MnCl_2 4H_2O$/kg. Mn concentration was determined using comparative NAA. Fe and Cu concentrations were determined using XRF. Statistical significance between control and treated groups at $p<0.05$ is denoted by the * symbol.

3.5 Manganese Discussion

In MEMRI studies, MR signal changes are attributed to the accumulation of manganese in the brain. However, the relaxivity of brain tissue can be altered by changes in other paramagnetic metals, such as copper and iron ions, in response to manganese increases in the brain. In this work, in addition to the expected manganese concentration increases in brain regions following high-dose manganese injections, a statistically significant decrease in iron concentration in the thalamus was found. In other brain regions copper and iron concentrations were also altered, although not significantly. These findings indicate that interpretation and analysis of manganese-enhanced MR images is complicated by disruptions in several transition metals.

The relaxation rates $R_1 = \frac{1}{T_1}$ and $R_2 = \frac{1}{T_2}$ of a paramagnetic ion in a water solution depend on the relaxivity $r_{1,2}$ and concentration of the ion $[\text{ion}]$ according to

$$R_{1\text{ or }2}(\text{ion}) = R_{1\text{ or }2}(0) + r_{1,2}[\text{ion}]$$

where $R_{1\text{ or }2}(0)$ is the relaxation of the water solution without the ion. When several paramagnetic ions are present in a solution, the effects of each ion on the relaxation rates are summated. For example, the longitudinal and transverse relaxation rates of a solution containing manganese and iron ions is

$$R_{1\text{ or }2}(\text{ions}) = R_{1\text{ or }2}(0) + r_{1,2}[Mn^{2+}] + r_{1,2}[Fe^{3+}]$$

When the concentrations of manganese and iron ions are known in a solution, the relaxivities of the metals can be measured and the MR relaxation rates and signal intensities can be determined. In vivo, however, the relationship between paramagnetic ion concentration and relaxation rates is more complex since the relaxivity of the metal changes with the surrounding environment and molecular form of the metal ion. For example, binding to intracellular ligands enhances the signal intensity on a T_1 weighted MR image, while changes to the metal electron structure or water access decrease the signal intensity (Kang, Gore, & Armitage, 1984). Furthermore, it has been proposed that the dependence of T_1 and T_2 values on manganese and iron levels in brain tissue is not linear but involves competition between the metals for common binding sites (Zhang et al., 2009). In order to determine the combined influence of the disrupted metal levels on the relaxation rates and signal intensities of manganese-enhanced MR images, the empirical relaxivities of each metal ion must be measured in each brain region. Using the competition model the authors estimated that the longitudinal relaxivities of bound manganese range between $0.25 - 7.65\ [\text{s/mmol kg tissue}]^{-1}$ in different brain regions and the longitudinal relaxivities of bound iron range between $0.07 - 1.15\ [\text{s/mmol kg tissue}]^{-1}$ in the rat brain at 4.7 Tesla (Zhang et al., 2009). In the present work the manganese concentration in the thalamus increased by $36\ \text{nmol/}\mu\text{g}$ while iron decreased by $122\ \text{nmol/}\mu\text{g}$. The relaxivity values of bound iron in the rodent brain and the large absolute decrease in the iron concentration indicate that both iron and manganese

must be considered when looking at signal changes in the thalamus on manganese-enhanced MR images. Changes in iron levels were also noted in other treated brain regions although not statistically significant, and caution should be taken when interpreting results for various brain regions in MEMRI studies.

Inter-regional differences in metal concentrations in the control mouse brain were observed in this work, although this was not the focus of the study. The thalamus iron and copper concentrations were significantly higher compared to the rest of the brain and the striatum respectively. No statistical differences in manganese concentrations across different regions in the brain were found. The regional distribution of metals in the manganese-treated mouse brains did not follow the same trends. Iron and copper concentrations were significantly higher in the treated white matter of the corpus callosum compared to the treated gray matter of the cortex, as well as treated hippocampus for copper. In addition, manganese accumulated in significantly higher concentrations in the treated thalamus and cerebellum compared to the cortex. These findings further suggest that there is metal dyshomeostasis in the mouse brain following high dose manganese injections.

The metal disruptions observed in this study contribute to findings of disruptions in other manganese studies. Decreased iron levels after brain over-exposure to manganese have been reported in a study where developing rats were exposed to a manganese-supplemented diet via maternal milk during lactation (Garcia et al., 2006). The study also reported an increase in the expression of metal transporter proteins, DMT-1 and transferrin receptor, in the brain. The regulation of manganese and iron transport by DMT-1 and transferrin receptor implies an inverse relationship between these metal levels. In addition, during manganese exposure the expression of an iron exporter protein ferroportin increases (Yin et al., 2010). Therefore, manganese accumulation in the brain would lead to decreases in iron we observed in various brain regions. Considering that the thalamus contains the greatest concentration of iron compared to other brain regions, it is not surprising that the largest and statistically significant decrease in iron occurred in this region following high-dose manganese injections.

Disruptions of metal homeostasis in the brain could be a result of systemic changes in metal levels in the blood and visceral organs, such as the kidney and liver. We did not find significant changes in the manganese levels in the blood between the control and manganese treated groups. However, since blood samples were drawn approximately 24 hours after the last manganese injection, it is possible that manganese was cleared from the blood in the treated animals by the time of collection. The liver and kidney both had a significantly higher manganese concentration in the manganese-treated mice. The manganese concentration in the liver increased 2.5 times and in the kidney 13 times, when comparing the metal levels of the treated to the control groups. The primary clearance mechanism of manganese is the liver via excretion in bile (Utter, 1976). Thus, the manganese concentration in the liver of the treated mice increased in the process of elimination of manganese from the body. The very large increase in the kidney could be explained by the accumulation of manganese in that organ as it is not the main route of manganese excretion. The copper and iron levels in the blood, kidney, and liver of manganese treated animals remained within the normal values of the control mice. The disruption of iron levels in the brain may be related to the accumulation of manganese in the brain only, rather than systemic changes in iron.

Overall, the change in iron levels in the thalamus following manganese injections in this study should serve as a caution that paramagnetic metal levels in the brain may be altered in MEMRI studies and that care should be taken when interpreting signal changes in brain regions where there may also be changes in other paramagnetic species following manganese injections. The decrease in iron we observed in the thalamus could be exacerbated at higher doses of injected manganese and decreases in iron could also become significant in other regions.

Chapter 4 – Cuprizone Experiment

4.1. Cuprizone Model of Demyelination

4.1.1 Myelin and Demyelination Disorders

The brain is primarily composed of two broad classes of cells: neurons and glial cells. Oligodendrocytes are glial cells in the central nervous system that are responsible for the formation of myelin, a specialized membrane used to insulate neurons. One oligodendrocyte cell ensheathes up to 60 separate axons (Miller, 2002) with multi-lamellar myelin, which enables electrical signals to be propagated rapidly and efficiently through saltatory conductance. Myelinated axons form the white matter in the brain which serves as a communication link between different brain regions. Effective communication between many brain areas is required during cognitive processing as sensory stimuli are received, compared with past experiences, and assessed at cognitive and emotional centers. It follows that the strength and organization of white matter in a brain area has been correlated to the performance on tasks specific for that brain area. For example, the organization of myelinated fibers in regions associated with musical ability correlate with the number of hours spent practicing the piano (Bengtsson et al., 2005). Conversely, poor cognitive and intellectual performance is related to white matter changes, such as the significantly smaller corpus callosum observed in severely neglected children (Teicher et al., 2004). White matter abnormalities result in cognitive deficits observed in several neurodegenerative disorders including multiple sclerosis.

Multiple sclerosis (MS) is a chronic inflammatory demyelinating disease of the central nervous system that destroys myelin, oligodendrocytes, axons, and neurons (Noseworthy, Lucchinetti, Rodriguez, & Weinshenker, 2000). The disease process underlying MS is often described by a combination of inflammatory and neurodegenerative models to explain differences in clinical presentation across the course of disease within an individual and between different patients (Bruck, 2007). The locations of white-matter lesions, the hallmarks of MS, determine the symptoms and severity of the disease in patients, which include motor-

related dysfunctions, cognitive impairment and decline, as well as dementia (Feinstein, Kartsounis, Miller, Youl, & Ron, 1992). Pathologically, the early stages of MS are characterized by acute inflammatory attacks, immune T-cell and astrocyte glial infiltration, axonal damage, and acute demyelination (Korn, 2008). After the initial stage of relapses and remissions, most MS patients enter a course of continuous neurological decline due to slow axonal damage of chronically demyelinated neurons (Korn, 2008).

4.1.2 The Cuprizone Animal Model

Cuprizone has been established as neurotoxic for mice (Carlton, 1966), guinea pigs and rats (Carlton, 1969), although demyelination may only occur in mice (Love, 1988). The first cuprizone experiments were performed in the 1960s showing lesions, edema, astrogliosis, and demyelination following dietary administration of the chemical to Swiss mice (Carlton, 1967). The basic model established that cuprizone-exposed mice show demyelination of several white matter tracts in a time frame of weeks, with the exact time course determined by the dose of cuprizone and age of the animals. Cuprizone is typically fed in the diet at concentrations 0.2-0.6% with severe weight loss and mortality rate rising in a dose dependent manner (Herring & Konradi, 2011). Following removal of cuprizone from the diet of mice with acute demyelination, substantial remyelination is observed within four to six weeks. After extended exposure to cuprizone for twelve weeks and chronic demyelination, remyelination is negligible as few fibers are remyelinated (Matsushima & Morell, 2001).

Cuprizone toxicity and the degree of demyelination have been shown to depend on mouse strain (Taylor, Gilmore, & Matsushima, 2009; Skripuletz et al., 2008), dose (Hiremath et al., 1998), anatomic location in the brain (Gudi et al., 2009), age (Kipp, Clarner, Dang, Copray, & Beyer, 2009), and gender (Taylor et al., 2009). However, feeding cuprizone to C57Bl/6 mice has been the preferred mouse strain for research due to the availability of the complete genome for this strain and possibility of knockout gene studies (Torkildsen, Brunborg, Myhr, & Bo, 2008). The pathology in the cuprizone model in C57Bl/6 mice is well characterized and highly reproducible. Following a 3 week exposure to cuprizone astrogliosis and oligodendrocyte apoptosis are observed with

demyelination evident after 4-6 weeks in multiple structures. Loss of myelin occurs primarily in the corpus callosum (Steelman, Thompson, & Li, 2012) but other affected brain areas include the hippocampus (Koutsoudaki et al., 2009), cerebellum (Groebe et al., 2009), external capsule (Pott et al., 2009), superior cerebellar peduncles (Ludwin, 1978), striatum (Pott et al., 2009), and cortex (Skripuletz et al., 2008; Gudi et al., 2009). During cuprizone exposure mice experience altered social interaction and impaired motor coordination (Hibbits, Pannu, Wu, & Armstrong, 2009), as well as liver toxicity. A standard treatment protocol of feeding 8-week-old C57Bl/6 mice with 0.2% cuprizone for 6 weeks has been shown to produce acute demyelination while minimizing hepatic toxicity and mortality rate of the mice (Torkildsen et al., 2008).

4.1.3 Mechanism of Action of Cuprizone

Cuprizone is a copper chelator and the observed pathology during administration of the chemical to mice is assumed, although not proven, to be due to binding of cuprizone to copper resulting in copper deficiency. In fact, the symptoms of genetic copper metabolism disorders, such as Menkes and Wilson diseases, are similar to those observed in the cuprizone model: growth retardation, hepatic failure, demyelination, and neurodegeneration (Madsen & Gitlin, 2007; Matsushima & Morell, 2001). Insufficiency of copper is thought to be detrimental to mitochondrial function in the brain, as well as in the liver, as copper is a co-factor of cytochrome oxidase, a key electron transport chain enzyme required for energy production through oxidative phosphorylation. In fact, cuprizone treated mice show inhibited cytochrome c oxidase activity in the brain and liver, and another mitochondrial enzyme, monoamine oxidase, is also inhibited (Venturi, 1973). Decreased copper ion levels in the whole mouse brain were also noted in this early study; and, administration of copper-chelated cuprizone to mice did not result in any enzymatic or ionic (Na^+, K^+, Cu^{2+}) changes compared to control animals (Venturi, 1973). Furthermore, the formation of megamitochondria in the liver of mice during cuprizone intoxication suggests a deficiency in mitochondrial function (Suzuki, 1969; Suzuki & Kikkawa, 1969). Taken together, these findings suggest that cuprizone toxicity results from cuprizone binding to copper; however, the administration of copper failed to reduce cuprizone-induced pathology (Carlton, 1967). During cuprizone intoxication oligodendrocytes

are the only brain cells that degenerate causing axonal demyelination, however abnormal morphology is also observed in astrocytes (Blakemore, 1972). It is not known why cuprizone does not cause degeneration of other cell types in the central nervous system. However, it has been hypothesized that a disturbance in energy metabolism during copper deficiency brought on by cuprizone is especially deleterious to myelin-producing oligodendrocytes because of their uniquely high energy requirements (Torkildsen et al., 2008).

There are two hypotheses that have been proposed to explain the action of cuprizone and how copper deficiency ensues. One hypothesis was postulated when the first studies on cuprizone were performed and states that cuprizone acts in the gut as a copper chelator (Venturi, 1973) causing a systemic copper deficiency; while the alternative hypothesis proposes that copper acts directly in the brain (Zatta et al., 2005). The current literature is conflicting with reports that support or refute the proposed cuprizone neurotoxic mechanisms. For example, the group that stated that cuprizone is toxic directly to brain cells based their hypothesis on the presence of cuprizone in the brain and liver of chronically cuprizone treated mice (Zatta et al., 2005). While another study investigated the physico-chemical properties and biological behaviour of cuprizone and the findings show that cuprizone is unable to pass through the mouse duodenal membrane and does not accumulate in the liver and brain of cuprizone-treated mice (Benetti et al., 2010). Furthermore, cuprizone and copper-cuprizone complex does not cross the neuronal plasma membrane, and does not alter the proliferation rate, cell cycle or viability of cultured neurons (Benetti et al., 2010). Also, the blood-brain barrier in cuprizone treated mice remains intact with no significant changes in permeability during demyelination development (Bakker & Ludwin, 1987). Since cuprizone is often administered to mice by being mixed into rodent chow, it is also possible that cuprizone chelates copper in the food and produces a copper deficient diet (Benetti et al., 2010).

In this study we investigated whether brain copper levels decrease in the commonly used protocol for the study of cuprizone-induced demyelination where C57Bl/6 mice are fed 0.2% cuprizone (w/w) for 6 weeks (Torkildsen et al., 2008). We also considered iron and manganese levels in the brain since their homeostasis is linked to copper. Transition

metal levels were also measured in blood, kidney, and liver tissue samples to assess possible systemic and visceral organ disruptions. X-ray fluorescence and neutron activation analysis techniques were used for metal measurements.

4.2 Cuprizone Treatment

The cuprizone experiment was carried out in 8-week-old male C57Bl/6 mice (Jackson Laboratories, ME). The treated (n=5) and control (n=5) groups of mice were allowed to acclimatize prior to onset of the experiment. All animals were kept on a 12 hour light/dark cycle and provided with food and water *ad libitum.* Cuprizone (Sigma, C9012) was milled into 8640 Teklad 22/5 rodent chow (Harlan Laboratories Inc., WI) at a concentration of 0.2% dry chemical to dry food weight and formed into half-inch pellets at Harlan Laboratories. The cuprizone rodent diet was kept in vacuum sealed bags, and opened containers were refrigerated until use.

The treated group of mice were housed five to a cage and fed the 0.2% cuprizone (w/w) diet for 6 weeks to induce demyelination. The weight and food intake were examined daily during the 6 week treatment. The control group of mice were housed four to a cage and fed the normal 8640 Teklad 22/5 Rodent Diet (Harlan Laboratories Inc., WI). All animals were sacrificed after the 6 week time-course.

4.3 Cuprizone Statistical Analysis

Statistical analyses were performed using SPSS software (IBM SPSS Statistics Version 20.0, IBM Corp.). Data was first assessed for normality using the Shapiro-Wilk test of normality. Levene's test of equality of error variances was then used to test the homogeneity of variances of the metal concentrations across groups. A two-way ANOVA followed by a Tukey HSD post-hoc test were used to test the significant differences in metal concentration between the brain regions of control and cuprizone treated mice. The significant differences in manganese, copper, and iron concentrations in the blood, liver, and kidney data were tested using independent T-tests. Independent T-tests were also used to test for significant differences in the weights of control and cuprizone treated mice at each week of treatment.

4.4 Cuprizone Experimental Results

During cuprizone treatment the mice were weighed and monitored for adverse health effects, such as listlessness, anorexia, ataxia, and tremors previously described during administration of cuprizone at higher doses (Stidworthy, Genoud, Suter, Mantei, & Franklin, 2003) (Hiremath, et al., 1998). The weight curve of the cuprizone treated mice is shown in Figure 14. During the first four weeks of cuprizone treatment there was no significant difference in body weights of control and treated mice ($p>0.05$) with both groups of mice gaining weight gradually. However, from five weeks until sacrifice the cuprizone treated mice had significantly lower body weights compared to control animals ($p<0.05$). During the experiment, the cuprizone treated mice did not present with any major abnormal clinical symptoms except for mild lethargy.

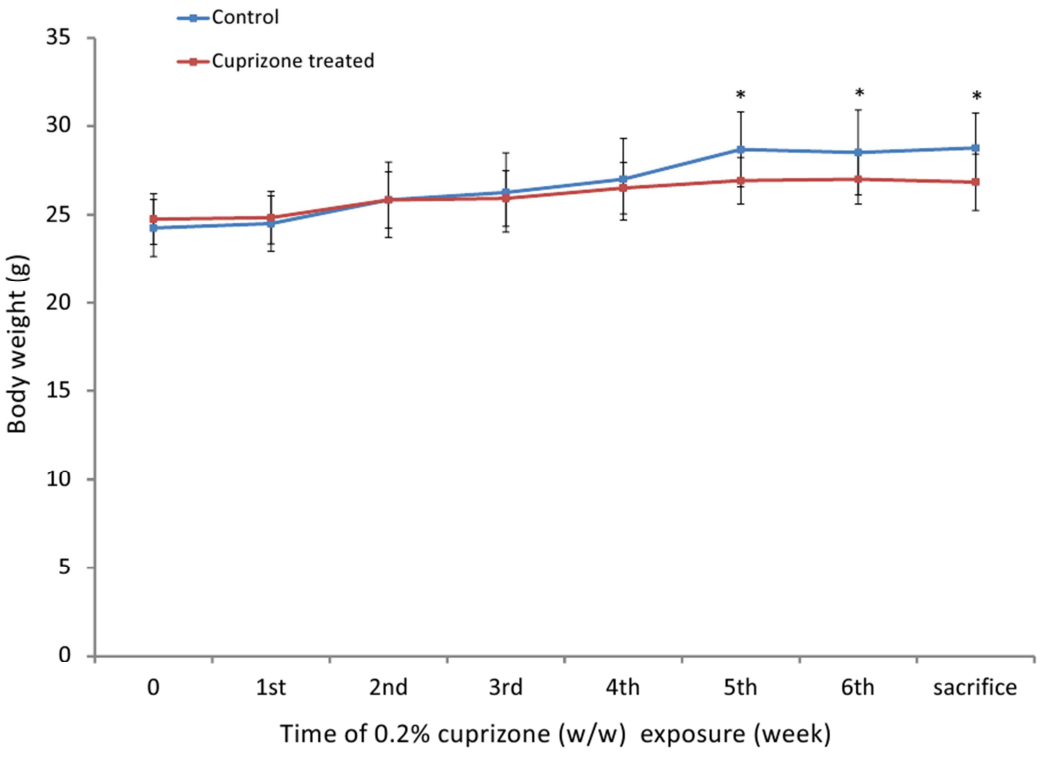

Figure 14. Effects of cuprizone treatment on body weight (mean ± std. dev., n=5 for each group) of C57Bl/6 mice treated with 0.2% cuprizone (w/w) for 6 weeks compared to control. Statistical significance between control and treated groups at $p<0.05$ is denoted by the * symbol.

Figure 15 shows the regional brain copper concentrations as measured with XRF in the control and cuprizone treated mice. Due to time restrictions, the control data shown in Figures 15, 16, and 17 consists of measurements done in the manganese study. This data was appropriate to use as control copper, iron, and manganese data in the brain in the cuprizone study since the control mice in both studies were of the same strain; sex and age matched; kept under the same conditions; and fed the same diet.

There was no significant change in the copper levels in the brains of mice treated with 0.2% cuprizone compared to the control group. Inter-regional differences in copper concentration were only significant between the control thalamus and striatum ($p<0.05$).

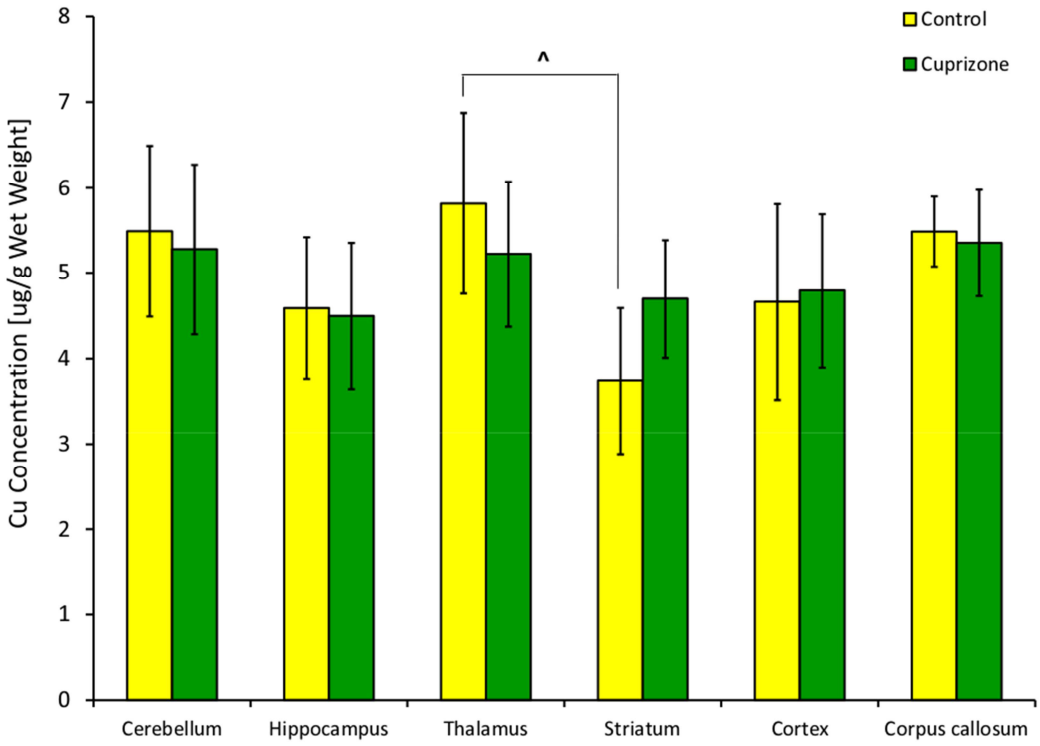

Figure 15. Copper concentration (mean ± std. dev., n=5 for each group) in different brain regions of C57Bl/6 control mice and mice treated with 0.2% cuprizone (w/w) for 6 weeks. Cu concentration was determined using XRF. Statistical significance between brain regions within the control group at $p<0.05$ is denoted by the ^ symbol.

The regional brain manganese concentrations measured with NAA in the control and mice fed a 0.2% cuprizone diet are given in Figure 16. Surprisingly, there was a significant increase in manganese in the hippocampus, cortex, and corpus callosum at the $p<0.05$ level of cuprizone treated mice compared to control.

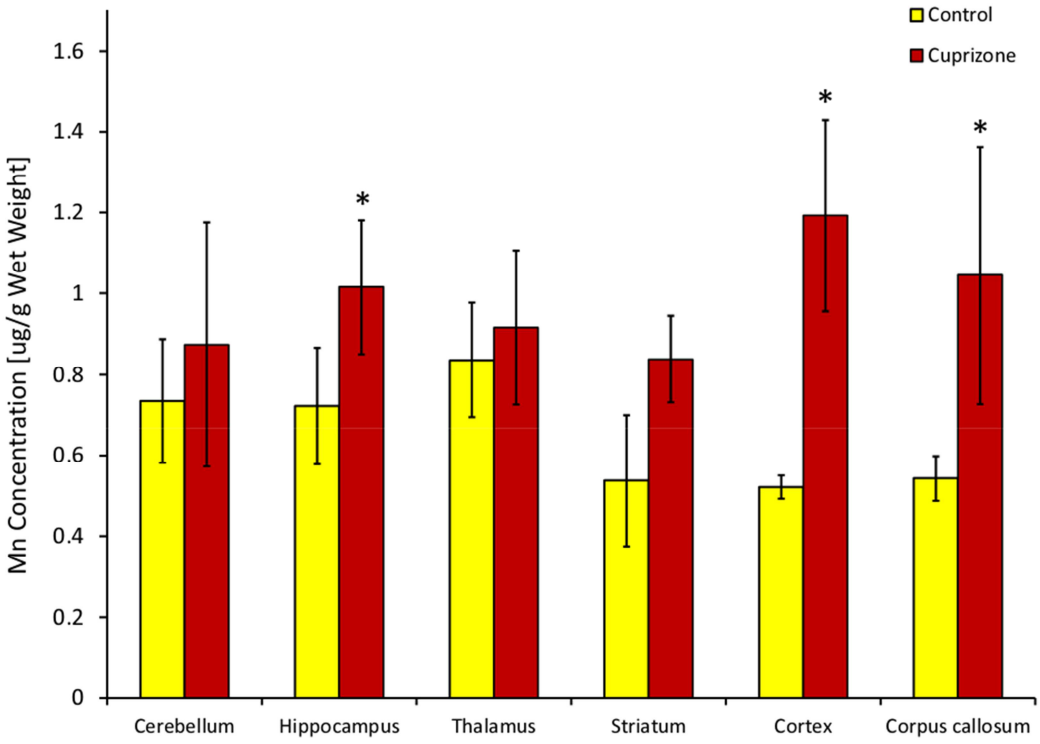

Figure 16. Manganese concentration (mean ± std. dev., n=5 for each group) in different brain regions of C57Bl/6 control mice and mice treated with 0.2% cuprizone (w/w) for 6 weeks. Mn concentration was determined using comparative NAA. Statistical significance between control and treated groups at $p<0.05$ is denoted by the * symbol.

Iron concentrations in the control and cuprizone treated mouse brain regions as measured with XRF are shown in Figure 17. There was no statistically significant changes in iron levels in the treated versus control mice ($p>0.05$). The iron concentration was significantly higher in the control thalamus than in the other five control brain regions at the $p<0.05$ level.

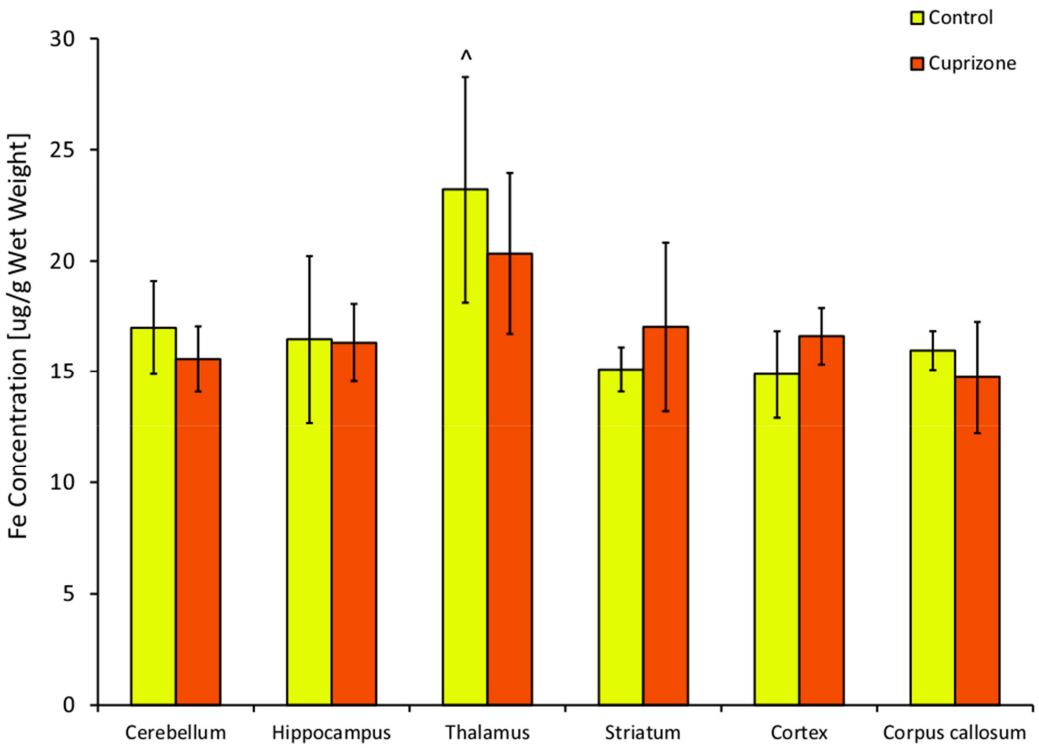

Figure 17. Iron concentration (mean ± std. dev., n=5 for each group) in different brain regions of C57Bl/6 control mice and mice treated with 0.2% cuprizone (w/w) for 6 weeks. Fe concentration was determined using XRF. Statistical significance between the five brain regions and the thalamus within the control group at $p<0.05$ is denoted by the ^ symbol.

In order to assess the circulating metal levels in the mice, blood was collected by cardiac puncture at the time of sacrifice and the measured copper, manganese, and iron levels are shown in Figure 18. The blood copper concentration was significantly lower in the cuprizone treated animals than in the controls at the $p<0.05$ level. The manganese and iron concentrations in the blood did not change significantly in the cuprizone treated animals compared to controls ($p>0.05$).

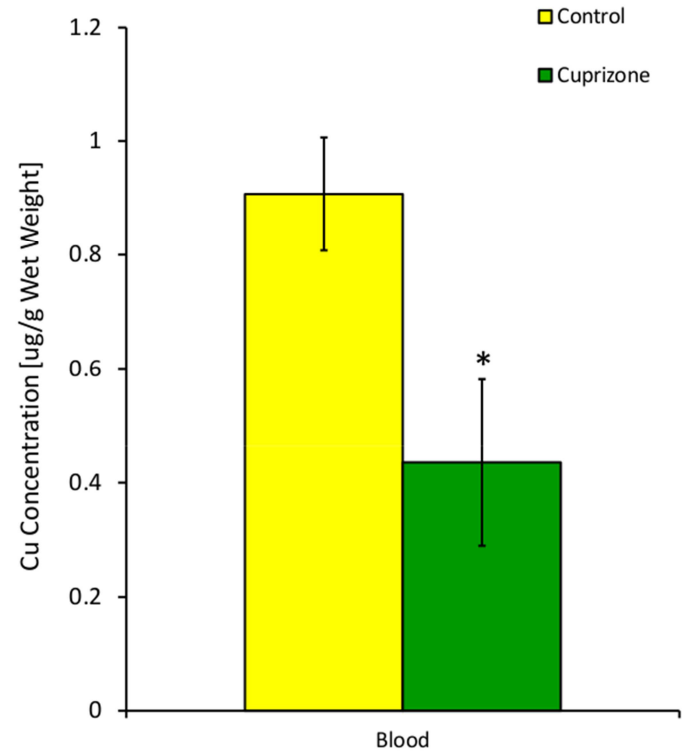
Control
Cuprizone
1.2
1
0.8
0.6
0.4
0.2
0
Cu Concentration [ug/g Wet Weight]
*
Blood

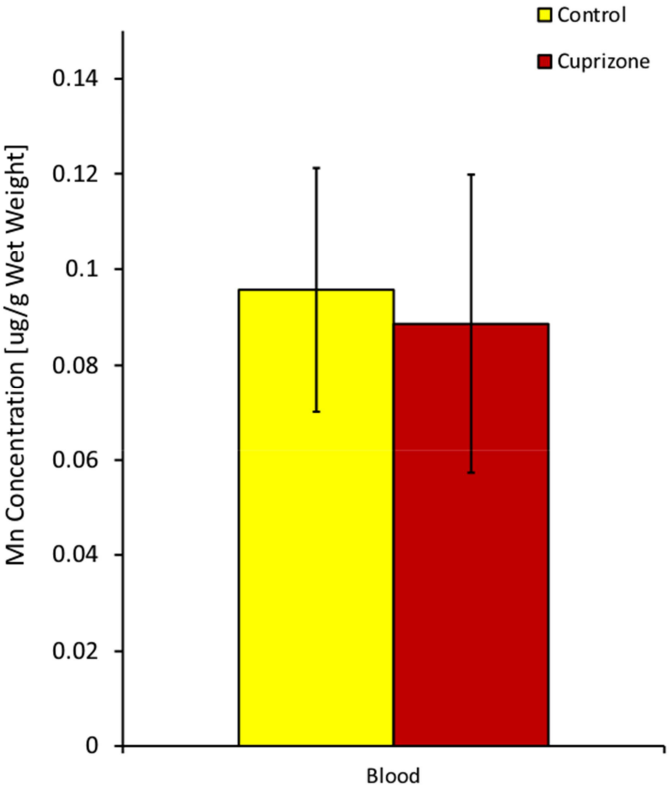
Control
Cuprizone
0.14
0.12
0.1
0.08
0.06
0.04
0.02
0
Mn Concentration [ug/g Wet Weight]
Blood

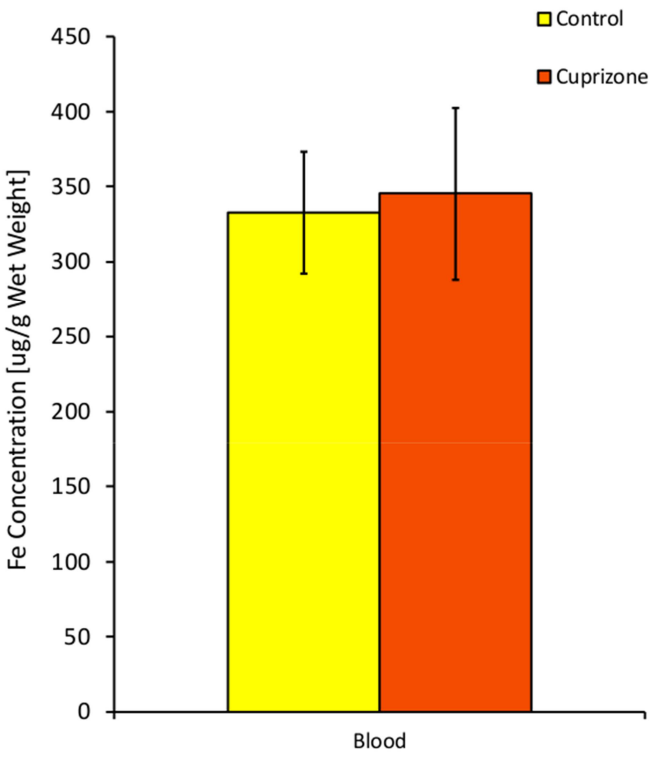

Figure 18. Copper, manganese, and iron concentrations (mean ± std. dev., n=5 for each group) in the blood of C57Bl/6 control mice and mice treated with 0.2% cuprizone (w/w) for 6 weeks. Cu and Fe concentrations were determined using XRF. Mn concentration was determined using comparative NAA. Statistical significance between control and treated groups at $p<0.05$ is denoted by the * symbol.

Figure 19 shows the copper, manganese, and iron levels in the visceral organs of cuprizone treated and control mice. The copper and manganese concentrations were significantly lower in the liver of the cuprizone treated animals compared to the control animals ($p<0.05$), while the iron concentration increased after cuprizone treatment in that organ ($p<0.05$). In the kidneys of cuprizone treated mice the copper and iron concentrations remained the same ($p>0.05$), while manganese concentration significantly decreased at the $p<0.05$ level compared to controls.

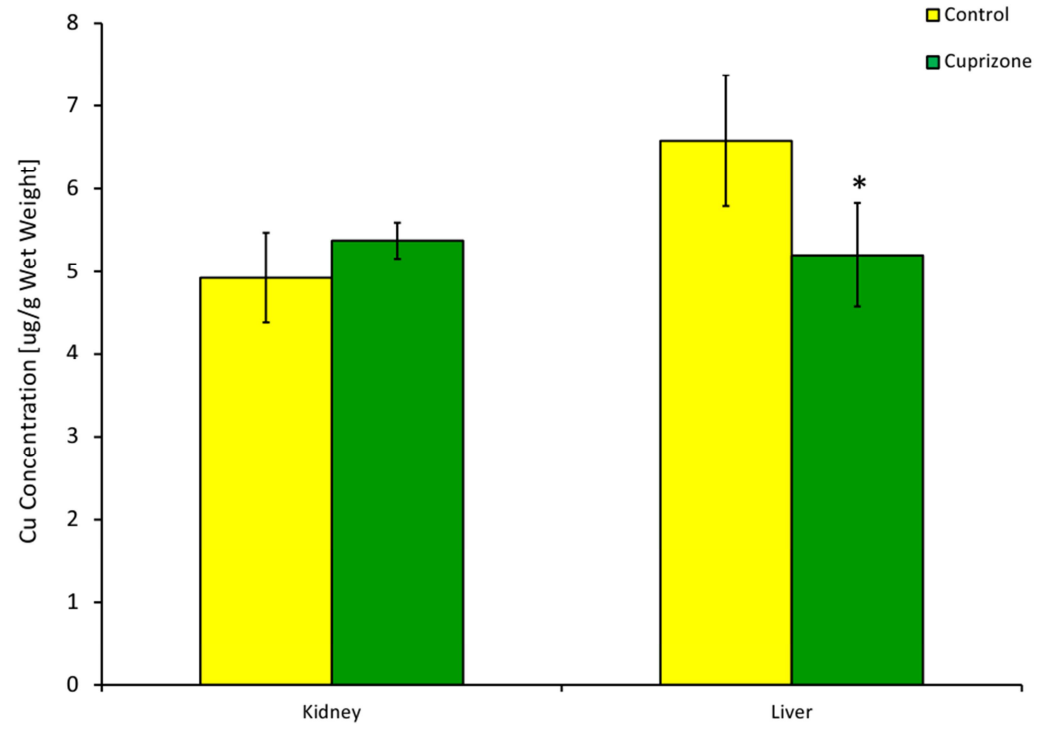
Control
Cuprizone
Cu Concentration [ug/g Wet Weight]
0
1
2
3
4
5
6
7
8
*
Kidney
Liver

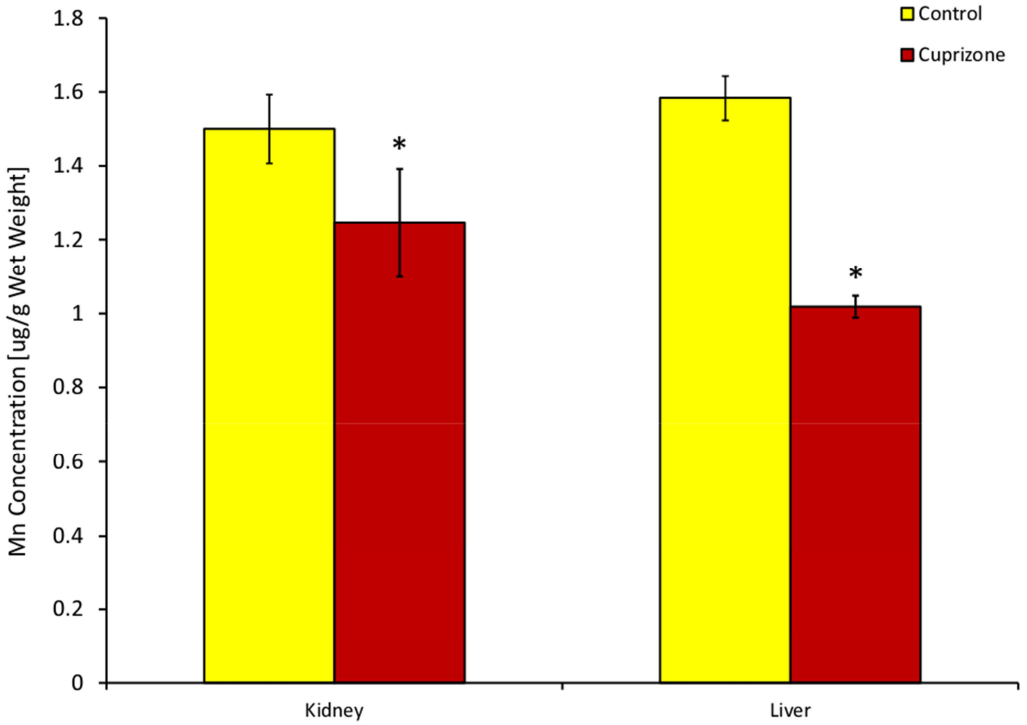
Control
Cuprizone
Mn Concentration [ug/g Wet Weight]
0
0.2
0.4
0.6
0.8
1
1.2
1.4
1.6
1.8
*
*
Kidney
Liver

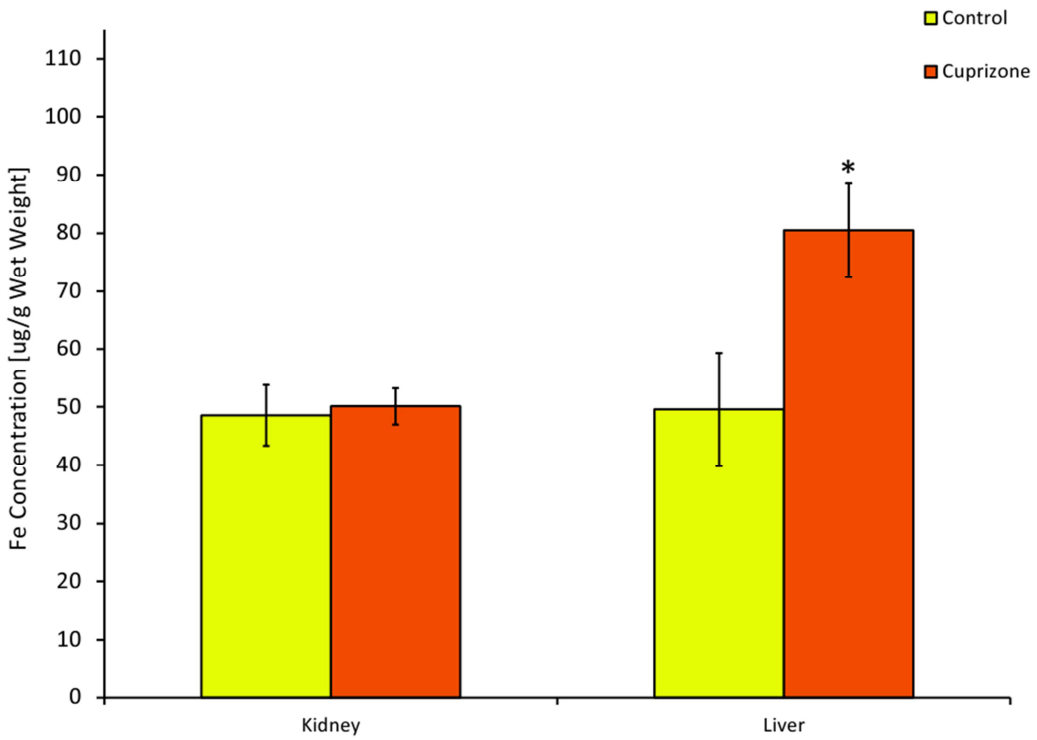

Figure 19. Copper, manganese, and iron concentrations (mean ± std. dev., n=5 for each group) in visceral organs of C57Bl/6 control mice and mice treated with 0.2% cuprizone (w/w) for 6 weeks. Cu and Fe concentrations were determined using XRF. Mn concentration was determined using comparative NAA. Statistical significance between control and treated groups at $p<0.05$ is denoted by the * symbol.

4.5 Cuprizone Discussion

The copper chelator cuprizone is a neurotoxin that causes demyelination. It is used as a model of multiple sclerosis where young adult mice are fed cuprizone to induce demyelination in the brain. The mechanism of cuprizone toxicity is not well-understood, although it is thought that chelation of copper by cuprizone and the resulting copper deficiency causes demyelination. The results in this work support the hypothesis that systemic copper levels are reduced during cuprizone treatment since copper levels were significantly decreased in the liver and blood of the cuprizone treated mice. Systemic copper homeostasis is primarily regulated by absorption of dietary copper in the small intestine followed by transport of copper ions to the kidneys and liver and binding to

ceruloplasmin in the liver to be released into the blood (Zheng & Monnot, 2012). It has been shown that cuprizone does not cross the transepithelial barrier in the small intestine suggesting that cuprizone chelates copper outside the body and reduces the amount of bioavailable copper ions in the small intestine (Benetti et al., 2010). The reduced copper levels in the liver and blood seen in this work may result from a lack of copper available for absorption in the small intestine and transport to the liver, as well as lower levels of copper-ceruloplasmin complex released into the blood. Other metals were also altered in the visceral organs with significant decreases of manganese in the treated liver and kidneys and significant increase of iron in the liver of the treated mice. Copper and manganese both function as co-factors in a group of free radical scavenging enzymes, SODs. In the face of copper deficiency in cuprizone induced toxicity, it is possible that the body tries to maintain manganese levels by decreasing excretion of the metal which may explain the decreased levels of manganese in the kidneys and liver. The increased iron levels in the liver were not unexpected since during severe copper deficiency iron transport within the body is deregulated and many tissues accumulate iron (Arredondo & Nunez , 2005). Furthermore, cuprizone toxicity in the liver has been established with morphological and biochemical alterations, such as formation of megamitochondria (Venturi, 1973; Russanov & Ljutakova, 1980). Since the liver is the main site of iron storage as well as accumulation of iron in diseased conditions, it is not surprising that iron levels increased in cuprizone treated mice.

The mechanism of neurotoxicity of cuprizone may be more complex than copper deficiency alone. If copper levels are imbalanced during cuprizone administration in mice, other transition metal levels may be altered as well. There have been limited studies with conflicting results that measured brain metal levels in different strains of mice and following varying treatment regimens with cuprizone. A study from the 1970's found decreased copper levels in whole brains of Swiss mice fed a 0.5% cuprizone diet for 3-4 weeks (Venturi, 1973). More recently, copper and zinc dyshomeostasis with increased levels of both metals in several brain regions was reported following chronic cuprizone treatment of CD mice for 3, 6, and 9 months with 0.2% cuprizone administration in drinking water (Zatta et al., 2005). This study investigated the metal levels in C57Bl/6 mice fed a 0.2% cuprizone diet for 6 weeks and the results show that

copper and iron levels did not change significantly in any of the brain regions examined, while manganese levels were significantly increased in the hippocampus, cortex, and corpus callosum. These findings suggest that the action of cuprizone in the brain is not simply an induced copper deficiency due to its copper chelation property as previously hypothesized. Despite the unchanged levels of copper in the brain the lower levels of copper in the blood and liver do suggest a copper deficiency in the cuprizone treated mice. However, the systemic copper deficiency may not be so severe as to cause decreased levels of copper in the brain since metal homeostasis in the brain is tightly regulated. It is interesting that manganese levels increased in the cuprizone treated hippocampus 1.4 times the control levels, treated cortex 2.3 times the control levels, and treated corpus callosum 1.9 times the control levels. An increase in the manganese concentration in the striatum was also observed although it was not statistically significant. Demyelination has been shown to occur in the corpus callosum (Steelman, Thompson, & Li, 2012), hippocampus (Koutsoudaki et al., 2009), cortex (Skripuletz et al., 2008; Gudi et al., 2009), and striatum (Pott et al., 2009) in the cuprizone model in C57Bl/6 mice corresponding to the brain areas with manganese concentration increases. Increased levels of manganese in these brain regions may be a compensatory mechanism for decreased systemic copper levels since manganese and copper are part of same classes of enzymes, such as MnSOD and CuZnSOD. Considering the neurotoxicity of elevated manganese levels in the brain, manganese may play a role in cuprizone-induced demyelination.

The mechanism of manganese neurotoxicity is two-fold: manganese directly affects cells by disrupting cellular metabolism and may also act indirectly by activation of glial cells (Filipov & Dodd, 2012). Manganese induced cellular dysfunction occurs when increased manganese levels are sequestered by mitochondria where manganese inhibits energy production and increases calcium levels, which leads to increased formation of reactive oxygen species (Gavin, Gunter, & Gunter, 1992; Gavin, Gunter, & Gunter, 1999). Furthermore, manganese disrupts energy production by directly inhibiting complexes I-IV – NADH dehydrogenase, succinate dehydrogenase, cytochrome bc_1 complex, and cytochrome c oxidase of the respiratory chain in brain mitochondria, as well as inhibiting monoamine oxidase mitochondrial enzyme

(Zhang, Zhou, & Fu, 2003). In the cuprizone demyelination model, it has been shown early on that the enzymatic activities of cytochrome c oxidase and monoamine oxidase are significantly reduced in the brain of cuprizone treated mice (Venturi, 1973). Therefore, it is the increased levels of manganese observed in this work rather than the hypothesized decreased copper levels in the brain that could explain the inhibition of these mitochondrial enzymes.

Manganese neurotoxicity has also been associated with manganese induced overactivation of glial cells, namely astrocytes and microglia, the support and immune cells in the CNS respectively (Spranger et al., 1998; Liu et al., 2009). Microglia and astrocytes normally have diverse beneficial functions essential for neuronal survival and importantly astrocytes have the ability to influence myelination by oligodendrocytes (Ishibashi et al., 2006); but overactivation of these cells is highly detrimental and neurotoxic (Zhao et al., 2009). Specifically, manganese activated astrocytes and microglia release various non-neuronal reactive oxygen species and numerous inflammatory mediators that contribute to degeneration of brain cells (Filipov & Dodd, 2012; Aschner, Erikson, Hernandez, & Tjalkens, 2009). In addition, manganese is highly toxic to astrocytes themselves (Aschner et al., 2009) because the metal accumulates in astrocytes in amounts 50 times greater than in neurons and severely disrupts astrocytic energy metabolism (Aschner, Gannon, & Kimelberg, 1992). The dysfunctional astrocytes may contribute to axonal loss and demyelination through oligodendrocyte damage and impaired myelination (Cambron et al., 2012). In the cuprizone model, microglial and astrocyte accumulation, as well as abnormal astrocytic morphology, was reported in several studies with the onset of demyelination and throughout the demyelinated areas in the cuprizone treated brains of mice (Pott et al., 2009; Hiremath et al., 1998; Blakemore, 1972). The invasion and proliferation of microglia and astrocytes correlated closely with demyelination in cuprizone toxicity in these studies. It is plausible then that the increased manganese concentrations in the corpus callosum, cortex, and hippocampus overactive astrocytes and microglia in these brain regions, as well as impair astrocytes themselves, causing detrimental neurotoxic effects that contributes to demyelination and pathologies observed during cuprizone exposure. Furthermore, remyelination and new oligodendrocytes have been observed in the cuprizone-treated brain when

the toxin is removed from the diet and the mice are allowed to recover (Matsushima & Morell, 2001). The restoration of myelin following toxic demyelination requires not only new oligodendrocytes but also the presence of astrocytes (Blakemore, 1984; Cambron et al., 2012). Removal of cuprizone may allow the brain to recover from the toxicity and re-establish manganese homeostasis, allowing astrocytes and oligodendrocytes to restore myelin sheaths on axons.

Overall, this study confirmed that systemic copper levels are reduced following cuprizone administration in C57Bl/6 mice since we saw decreased copper levels in the liver and blood of the cuprizone treated mice. Effects of cuprizone toxicity in the liver were also observed as we saw significantly increased iron levels in that organ. However, copper levels, as well as iron levels, remained unchanged in the brains of cuprizone treated mice. Surprisingly, it was manganese concentrations that were significantly higher in several brain regions that are known to demyelinate in this model. We propose a mechanism of cuprizone toxicity where manganese neurotoxicity contributes to demyelination through activation of microglia and astrocytes, as well as disruption of astrocytes themselves.

Chapter 5 – Future Works

5.1. Manganese Experiment

The MEMRI study investigated the regional metal levels in the brain as well as visceral organs after over-exposure to manganese. We found significantly decreased iron levels in the thalamus of high-dose manganese treated mice that could affect MRI contrast in MEMRI studies. In order to elucidate the effect of decreased iron and increased manganese concentrations in MEMRI studies further experiments are needed. For example, MRI studies are crucial to look at the individual contributions of iron and manganese to the MR signal in MEMRI in addition to the metal measurements made in this work. While it is hard to determine the intrinsic relaxivities of iron and manganese in vivo, qualitative images can be obtained to substantiate the results of our study. Specifically, MRI can be performed in mice that receive manganese injections but are kept on an iron deficient or iron supplemented diet in order to try and discern the effect of each metal. Proper controls in this experiment would consist of untreated control mice, control mice kept on an iron-deficient diet and control mice kept on an iron-supplemented diet. If metal concentrations and MRI images are measured in such a study, the exact effect of changing iron concentrations following manganese injections may be determined. Other follow-up studies may investigate metal homeostasis in the mouse brain following different manganese dosing protocols, such as higher and lower doses or different injections periods that may be used in MEMRI experiments.

5.2. Cuprizone Experiment

The cuprizone study investigated metal homeostasis in the brain, as well as systemically, in the C57Bl/6 mouse model of 0.2% cuprizone intoxication for 6 weeks. Of most importance, we found decreased systemic copper levels and increased manganese levels in the treated corpus callosum, cortex, and hippocampus, as well as increased iron levels in the cuprizone impaired liver. However, our data set for the statistical analysis of copper, iron, and manganese levels in the brain included control measurements from the manganese study since there

was not enough time to complete all the measurements for this work. Thus, XRF measurements on the control brain regions of mice from the cuprizone study must be made and analysed for copper and iron concentrations. Then, NAA samples must be prepared from the brain tissue in XRF holders and measured for manganese content.

The results show disruptions in metal levels in the brain, organs, and blood of cuprizone treated mice; however, histology must be done in order to confirm demyelination in the treated mice. Two groups of C57Bl/6 mice, one group as healthy controls and another group treated with 0.2% cuprizone for 6 weeks are required for histological analysis.

Our results suggest that cuprizone chelates copper in the small intestine causing copper deficiency in the body which results in altered transition metal levels that may be part of the mechanism of cuprizone toxicity. It was previously shown in CD1 mice fed 0.5% cuprizone diet for 16 days that cuprizone does not enter the body through the small intestine and that it is not present in brain and liver tissues (Benetti et al., 2010). These findings should be confirmed in the model used in this study, 8-week-old C57Bl/6 mice fed 0.2% cuprizone for 6 weeks. The brain, kidney, liver, and blood control and treated tissue samples prepared during the cuprizone study can be analysed using mass spectrometry for cuprizone content.

5.3. Overall Conclusion

This thesis demonstrated the measurement of the transition metals iron, copper, and manganese, in order to better understand their role in neurological disease. XRF and NAA techniques were successfully applied to make metal measurements in very small fresh brain tissue samples from rodents. This research work consisted of two experiments where altered transition metals were observed in the brains of mice, as well as visceral organs. In a manganese-enhanced MRI study looking at transition metal homeostasis following manganese injections, increased iron levels were observed in the thalamus which may affect MR contrast in MEMRI studies. In a demyelination model looking at transition metal homeostasis following cuprizone, a copper chelator, administration, increased manganese levels were found in the corpus callosum, cortex, and

hippocampus brain regions which may explain the neurotoxic action of cuprizone.

The measurements developed in this work have many applications in neurodegenerative diseases in which altered metal levels have been implicated, such as Alzheimer's disease, Parkinson's disease, and others. Importantly, these techniques can be used not only in rodent but in human tissue. Many studies have a need for investigation of metal levels where XRF and NAA techniques can be applied to elucidate changes in metal levels in disease.

References

Abreu, I. A., & Cabelli, D. E. (2010). Superoxide dismutases-a review of the metal-associated mechanistic variations. *Biochimica et Biophysica Acta, 1804*, 263-274.

Afonso, C., Lee, J. H., Aoki, I., & Koretsky, A. (2004). Manganese-enhanced magnetic resonance imaging (MEMRI): methodological and practical considerations. *NMR in Biomedicine, 17*, 532-543.

Aoki, I., Naruse, S., & Tanaka, C. (2004). Manganese-enhanced magnetic resonance imaging (MEMRI) of brain activity and applications to early detection of brain ischemia. *NMR in Biomedicine, 8*, 569-580.

Arredondo , M., & Nunez , M. T. (2005). Iron and copper metabolism. *Molecular Aspects of Medicine, 26*, 313-327.

Aschner, M., Erikson, K. M., & Dorman, D. C. (2005). Manganese dosimetry: species differences and implications for neurotoxicity. *Critical Reviews in Toxicology, 35*, 1-32.

Aschner, M., Erikson, K. M., Hernandez, E. H., & Tjalkens, R. (2009). Manganese and its role in parkinson's disease: from transport to neuropathology. *NeuroMolecular Medicine, 11*, 252-266.

Aschner, M., Gannon, M., & Kimelberg, H. K. (1992). Manganese uptake and efflux in cultured rat astrocytes. *Journal of Neurochemistry, 58*, 730-735.

Bakker, D. A., & Ludwin, S. K. (1987). Blood-brain barrier permeability during cuprizone-induced demyelination. *Journal of the Neurological Sciences, 78*, 125-137.

Beard, J. L., Connor, J. R., & Jones, B. C. (1993). Iron in the brain. *Nutrition Reviews, 51*(6), 157-170.

Benetti, F., Ventura, M., Salmini, B., Ceola, S., Carbonera, D., Mammi, S., . . . Spisni, E. (2010). Cuprizone neurotoxicity, copper deficiency and neurodegeneration. *Neurotoxicology, 31*, 509-517.

Bengtsson, S. L., Nagy, Z., Skare, S., Forsman, L., Forssberg, H., & Ullen, F. (2005). Extensive piano practicing has regionally specific effects on white matter development. *Nature Neuroscience, 8*, 1148-1150.

Blakemore, W. (1972). Observations on oligodendrocyte degeneration, the resolution of status spongiosus and remyelination in the cuprizone intoxication in mice. *Journal of Neurocytology, 1*, 413-426.

Blakemore, W. (1984). The response of oligodendrocytes to chemical injury. *Acta Neurologica Scandinavica Supplementum, 100*, 33-38.

Bloch, F., Hansen, W. W., & Packard, M. (1946). The nuclear induction experiment. *Phys. Rev*, 474-485.

Bloembergen, N., Purcell, E. M., & Pound, R. V. (1948). Relaxation effects in nuclear magnetic resonance absorption. *Phys. Rev.*, 679-712.

Bock, N. A., & Silva, A. C. (2007). Manganese: a unique neuroimaging contrast agent. *Future Neurology, 2*(3), 297-305.

Bock, N., Kocharyan, A., & Silva, A. (2009). Manganese-enhanced MRI visualizes V1 in the non-human primate visual cortex. *NMR in Biomedicine, 22*(7), 730-736.

Bock, N., Paiva, F., & Silva A. (2008). Fractionated manganese-enhanced magnetic resonance imaging. *NMR in Biomedicine, 21*, 473-478.

Bruck, W. (2007). New insights into the pathology of multiple sclerosis: towards a unified concept. *Journal of Neurology, 254 [Suppl 1]*, I/3-I/9.

Burhans , M. S., Dailey , C., Beard, Z., Wiesinger , J., Murray-Kolb , L., Jones , B. C., & Beard , J. L. (2005). Iron deficiency: differential effects on monoamine transporters. *Nutritional Neuroscience, 8*, 31-38.

Cambron, M., D'haeseleer, M., Laureys, G., Clinckers, R., Debruyne, J., & De Keyser, J. (2012). White-matter astrocytes, axonal energy metabolism, and axonal degeneration in multiple sclerosis. *Journal of Cerebral Blood Flow and Metabolism, 32*, 413-424.

Canavan, M., Cobb, S., & Drinker, C. (1934). Chronic manganese poisening: report of a case, with autopsy. *Archives of Neurology and Psychiatry, 32*, 501-512.

Carlton, W. W. (1966). Response of mice to the chelating agents sodium diethyldithiocarbamate, alpha-benzoinoxime and biscyclohexane oxaldihydrozone. *Toxicology and Applied Pharmacology, 8*, 512-521.

Carlton, W. W. (1967). Studies on the induction of hydrocephalus and spongy degeneration by cuprizone feeding and attempts to antidote the toxicity. *Life Sciences, 6*, 11-19.

Carlton, W. W. (1969). Spongiform encephalopathy induced in rats and guinea pigs by cuprizone. *Experimental and Molecular Pathology, 10*, 274-287.

Chaki, H., Furuta, S., Matsuda, A., Yamauchi, K., Yamamoto, K., Kokuba, Y., & Fujibayashi, Y. (2000). Magnetic resonance image and blood manganese concentration as indices for manganese content in the brain of rats. *Biological Trace Element Research, 74*, 245-257.

Chandra, S. V., & Shukla, G. S. (1967). Role of iron deficiency in inducing susceptibility to manganese toxicity. *Archives of Toxicology, 35*, 319-323.

Chen, M. T., Cheng, G. W., Lin, C. C., Chen , B. H., & Huang, Y. L. (2006). Effects of acute manganese chloride exposure on lipid peroxidation and alteration of trace metals in rat brain. *Biological Trace Element Research, 110*, 163-177.

Chua, A., & Morgan, E. H. (1996). Effects of iron deficiency and iron overload on manganese uptake and deposition in the brain and other organs of the rat. *Biological Trace Element Research, 55*, 39-54.

Donnelly, P. S., Xiao, Z., & Wedd, A. G. (2007). Copper and Alzheimer's disease. *Current Opinion in Chemical Biology, 11*, 128-133.

Erikson, K. M., Syversen, T., Steinnes, E., & Aschner, M. (2004). Globus pallidus: a target brain region of divalent metal accumulation associated with dietary iron deficiency. *Journal of Nutritional Biochemistry, 15*, 335-341.

Erikson, K. M., Thompson, K., Aschner, J., & Aschner, M. (2007). Manganese neurotoxicity: a focus on the neonate. *Pharmacology & Therapeutics, 113*, 369-377.

Feinstein, A., Kartsounis, L. D., Miller, D. H., Youl, B. D., & Ron, M. A. (1992). Clinically isolated lesions of the type seen in multiple sclerosis: a cognitive, psychiatric, and MRI follow up study. *Journal of Neurology, Neurosurgery, and Psychiatry, 55*, 869-876.

Filipov, N. M., & Dodd, C. A. (2012). Role of glial cells in manganese neurotoxicity. *Applied Toxicology, 32*, 310-317.

Fitsanakis, V., Zhang, N., Garcia, S., & Aschner, M. (2010). Manganese (Mn) and iron (Fe): interdependency of transport and regulation. *Neurotoxicity Research, 18*, 124-131.

Fleming, M. D., Trenor, C. C., Su, M. A., Foernzler, D., Beier, D. R., Dietrich, W. F., & Andrews, N. C. (1997). Microcytic anaemia mice have a mutation in Nramp2, a candidate iron transporter gene. *Nature Genetics, 16*, 383-386.

Fujita, M., Itakura, T., Takagi, Y., & Okaga, A. (1989). Copper deficiency during total parenteral nutrition: clinical analysis of three cases . *Journal of Parenteral and Enteral Nutrition, 13*, 421-425.

Gaasch, J. A., Lockman, P. R., Geldenhuys, W. J., Allen, D. D., & Van der Schyf, C. J. (2007). Brain iron toxicity: differential responses of astrocytes, neurons, and endothelial cells. *Neurochemical Research, 32*, 1196-11208.

Garcia, S. J., Gellein, K., Syversen, T., & Aschner, M. (2006). A manganese-enhanced diet alters brain metals and transporters in the developing rat. *Toxicological Sciences, 92*(2), 516-525.

Garrick, M. D., Dolan, K. G., Horbinski, C., Chio , A. J., Higgins, D., Porubcin, M., . . . Conrad, M. E. (2003). DMT1: a mammalian transporter for multiple metals. *Biometals, 16*, 41-54.

Gavin, C. E., Gunter, K. K., & Gunter, T. E. (1992). Mn2+ sequestration by mitochondria and inhibition of oxidative phosphorylation. *Toxicology and Applied Pharmacology, 115*, 1-5.

Gavin, C. E., Gunter, K. K., & Gunter, T. E. (1999). Manganese and calcium transport in mitochondria: implications for manganese toxicity. *Neurotoxicology, 20*, 445-453.

Groebe, A., Clarner, T., Baumgartner, W., Dang, J., Beyer, C., & Kipp, M. (2009). Cuprizone treatment induces distinct demyelination, astrocytosis, and microglia cell invasion or proliferation in the mouse cerebellum. *Cerebellum, 8*, 163-174.

Grodstein, G. W. (1957). *X-ray attenuation coefficients from 10 keV-100 Mev.* Washington: National Bureau of Standards Circular 583.

Grunecker, B., Kaltwasser, S. F., Peterse, Y., Samann, P., Schmidt, M., Wotjak, C., & Czisch, M. (2010). Fractionated manganese injections: effects on MRI contrast enhancement and physiological measures in C57BL/6 mice. *NMR in Biomedicine, 23*, 913-921.

Gudi, V., Moharregh-Khiabani, D., Skripuletz, T., Koutsoudaki, P. N., Kotsiari, A., Skuljec, J., . . . Stangel, M. (2009). Regional differences between grey and white matter in cuprizone induced demyelination. *Brain Research, 1283*, 127-138.

Gunshin, H., Mackenzie, B., Berger, U., Gunshin, Y., Romero, M., Boron, W., . . . Hediger, M. (1997). Cloning and characterization of a mammalian proton-coupled metal-ion transporter. *Nature, 388*, 482-488.

Heggie, J. C., Liddell, N. A., & Maher, K. P. (2001). *Applied imaging technology.* Melbourne: St Vincent's Hospital.

Herring, N. R., & Konradi, C. (2011). Myelin, copper, and the cuprizone model of schizophrenia. *Frontiers in Bioscience, 3*, 23-40.

Hibbits, N., Pannu, R., Wu, J. T., & Armstrong, R. C. (2009). Cuprizone demyelination of the corpus callosum in mice correlates with altered social interaction and impaired bilateral sensorimotor coordination. *ASN Neuro, 1(3)*, 153-164.

Hiremath, M. M., Saito, Y., Knapp, G. W., Ting, J. P., Suzuki, M., & Matsushima, G. K. (1998). Microglial/macrophage accumulation during cuprizone-induced demyelination in C57BL/6 mice. *Journal of Neuroimmunology, 92*, 38-49.

Ishibashi, T., Dakin, K. A., Stevens, B., Lee, P. R., Kozlov, S. V., Stewart, C. L., & Fields, D. R. (2006). Astrocytes promote myelination in response to electrical impulses. *Neuron, 49*, 823-832.

Jarekt. (2007). *Mass attenuation coefficient of iron with contributions sources of attenuation data.* Retrieved from XCOM database.

Kang, Y. S., Gore, J. C., & Armitage, A. M. (1984). Studies of factors affecting the design of NMR contrast agents: manganese in blood as a model system. *Magnetic Resonance in Medicine, 3*, 396-409.

Kim , Y., Kim, K. S., Yang , J. S., Park, I. J., Kim, E., Kwon, K. R., . . . Moon, Y. (1999). Increase in signal intensities on T1-weighted magnetic resonance images in asymptomatic manganese-exposed workers. *Neurotoxicology, 20*(6), 901-907.

Kim, Y. (2004). High signal intensities on T1-weighted MRI as a biomarker of exposure to manganese. *Industrial Health, 42*(2), 111-115.

Kipp, M., Clarner, T., Dang, J., Copray, S., & Beyer, C. (2009). The cuprizone animal model: new insights into an old story. *Acta Neuropathologica, 118*, 723-736.

Knoll, G. F. (2000). *Radiation detection and measurement.* John Wiley & Sons Inc.

Koretsky, A. P., & Silva, A. C. (2004). Manganese-enhanced magnetic resonance imaging (MEMRI). *NMR in Biomedicine, 17*(8), 527-531.

Korn, T. (2008). Pathophysiology of multiple sclerosis. *Journal of Neurology, 255 [Suppl 6]*, 2-6.

Koutsoudaki, P. N., Skripuletz, T., Gudi, V., Moharregh-Khiabani, D., Hildebrandt, H., Trbst, C., & Stangel, M. (2009). Demyelination of the hippocampus is prominent in the cuprizone model. *Neuroscience Letters, 451*, 83-88.

Lai, J. C., Minski, M. J., Chan, A. W., Leung, T. K., & Lim, L. (1999). Manganese mineral interactions in brain. *Neurotoxicology, 20*, 433-444.

Lechner, P., Fiorini, C., Longoni, A., Lutz, G., Pahlke, A., Soltau, H., & Struder, L. (2004). Silicon drift detectors for high resolution, high count rate X-ray spectroscopy at room temperature. *International Centre for Diffraction Data, Advances in X-ray Analysis, 47*, 53-58.

Liu, M., Cai, T., Zhao, F., Zheng, G., Wang, Q., Chen, Y., . . . Chen, J. (2009). Effect of microglia activation on dopaminergic neuronal injury induced by manganese, and its possible mechanism. *Neurotoxicology Research, 16*, 42-49.

Love, S. (1988). Cuprizone neurotoxicity in the rat: morphologic observations. *Journal of Neurological Sciences, 84*, 223-237.

Ludwin, S. K. (1978). Central nervous system demyelination and remyelination in the mouse. An ultrastructural study of cuprizone toxicity. *Laboratory Investigation, 39*, 597-612.

Madsen, E., & Gitlin, J. D. (2007). Copper and iron disorders of the brain. *Annual Reviews of Neuroscience, 30*, 317-337.

Matsushima, G. K., & Morell, P. (2001). The neurotoxicant, cuprizone, as a model to study demyelination and remyelination in the central nervous system. *Brain Pathology, 11*, 107-116.

Miller, M. C. (1991). X-ray fluorescence. In D. Reilly, B. Ensslin, H. J. Smith, & S. Kreiner, *Passive nondestructive assay of nuclear material* (pp. 313-335). United States Nuclear Regulatory Commission.

Miller, R. H. (2002). Regulation of oligodendrocyte development in the vertebrate CNS. *Progress in Neurobiology, 67*, 451-467.

Mughabghab, S. F. (2003). *Thermal neutron capture cross sections resonance integrals and G factors.* Vienna: International Nuclear Data Committee IAEA.

Normandin, L., Beaupre, L. A., Salehi, F., St. Pierre, A., Kennegy, G., Mergler, D., . . . Zayed, J. (2004). Manganese distribution in the brain and neurobehavioral changes following inhalation exposure of rats to three chemical forms of manganese. *Neurotoxicology, 25*, 433-441.

Noseworthy, J. H., Lucchinetti, C., Rodriguez, M., & Weinshenker, B. G. (2000). Multiple sclerosis. *The New England Journal of Medicine, 343*, 938-952.

Pal, P. K., Samii , A., & Calne , D. B. (1999). Manganese neurotoxicity: a review of clinical features, imaging and pathology. *Neurotoxicology, 20*, 227-238.

Pautler, R., Silva, A., & Koretsky, A. (1998). In vivo neuronal tract tracing using manganese-enhanced magnetic resonance imaging. *Magnetic Resonance Imaging, 5*, 740-748.

Pidruczny, A., Butler, M., Ernst, P., Collins, M. F., & Avelar , J. M. (1994). The McMaster University nuclear reactor (MNR) research facilities. *Journal of Radioanalytical and Nuclear Chemistry, 180*, 313-318.

Pott, F., Gingele, S., Clarner, T., Dang, J., Baumgartner, W., Beyer, C., & Kipp, M. (2009). Cuprizone effect on myelination, astrogliosis and microglia attraction in the mouse basal ganglia. *Brain Research, 1305*, 137-149.

Roels, H., Lauwerys, R., Genet, P., Sarham, M. J., de Fays, M., Hanotiau, I., & Buchet , j. P. (1987). Relationship between external and internal parameters of exposure to manganese in workers from a manganese oxide and salt producing plant. *American Journal of Industrial Medicine, 11*, 297-305.

Roos, C. E. (1957). K fluorescence yield of several metals. *Physical Review, 105*, 931-935.

Russanov, E. M., & Ljutakova, S. G. (1980). Effect of cuprizone on copper exchange and superoxide dismutase activity in rat liver. *General Pharmacology, 11*, 535-538.

Sahni , V., Leger, Y., Panaro, L., Allen , M., Giffin , S., Fury, D., & Hamm, N. (2007). Case report: a metabolic disorder presenting as pediatric manganism. *Environmental Health Perscpectives, 115*, 1176-1179.

Schrag, M., Dickson, A., Jiffry, A., Kirsch, D., Vinters, H. V., & Kirsch, W. (2010). The effect of formalin fixation on the levels of brain transition metals in archived samples. *Biometals, 23*, 1123-1127.

Sheuhammer, A. M., & Cherian, M. G. (1981). The influence of manganese on the distribution of essential trace elements. *Toxicology and Applied Pharmacology, 61*, 227-233.

Shin, Y. C., Kim, E., Cheong, H., Cho, S., Sakong, J., Kim, K. S., . . . Kim, Y. (2007). High signal intensity on magnetic resonance imaging as a predictor of neurobehavioral performance of workers exposed to manganese. *Neurotoxicology, 2*, 257-262.

Silva, A. C., Lee, J. H., Aoki, I., & Koretsky, A. P. (2004). Manganese-enhanced magnetic resonance imaging (MEMRI): methodological and practical considerations. *NMR in Biomedicine*, 532-543.

Silva, A., Lee, J., Tucciarone, J., Pelled, G., Aoki, I., & Koretsky, A. (2008). Detection of cortical laminar architecture using manganese-enhanced MRI. *Journal of Neuroscience Methods, 2*, 246-257.

Skripuletz, T., Lindner, M., Kotsiari, A., Garde, N., Fokuhl, J., Linsmeier, F., . . . Stangel, M. (2008). Cortical demyelination is prominent in the murine cuprizone model and is strain-dependent. *American Journal of Pathology, 172*, 1053-1061.

Spranger, M., Schwab, S., Desiderato, S., Bonmann, E., Krieger, D., & Fandrey, J. (1998). Manganese augments nitric oxide synthesis in murine astrocytes: a new pathogenetic mechanism in manganism? *Experimental Neurology, 149*, 277-283.

Steelman, A. J., Thompson, J. P., & Li, J. (2012). Demyelination and remyelination in anatomically distinct regions of the corpus callosum following cuprizone intoxication. *Neuroscience Research, 72*, 32-42.

Stidworthy, M., Genoud, S., Suter, U., Mantei, N., & Franklin, R. J. (2003). Quantifying the early stages of remyelination following cuprizone-induced demyelination. *Brain Pathology, 13*, 329-339.

Suzuki, K. (1969). Giant hepatic megamitochondria: production in mice fed with cuprizone. *Science, 163*, 81-82.

Suzuki, K., & Kikkawa, T. (1969). Status spongiosus of CNS and hepatic changes induced by cuprizone (biscyclohexanone oxalyldihydrazone). *American Journal of Pathology, 54*, 307-325.

Taylor, L. C., Gilmore, W., & Matsushima, G. K. (2009). SJL mice exposed to cuprizone intoxication reveal strain and gender pattern differences in demyelination. *Brain Pathology, 19*, 467-479.

Teicher, M. H., Dumont, N. L., Ito, Y., Vaituzis, C., Giedd, J. N., & Andersen, S. L. (2004). Childhood neglect is associated with reduced corpus callosum area. *Biological Psychiatry, 56*, 80-85.

Torkildsen, O., Brunborg, L. A., Myhr, K. M., & Bo, L. (2008). The cuprizone model for demyelination. *Acta Neurologica Scandinavica, 117*, 72-76.

Utter, M. F. (1976). The biochemistry of manganese. *The Medical Clinics of North America, 60*(4), 713-727.

Van der Linden, A., Van Meir, V., Tindemans, I., Verhoye, M., & Balthazart, J. (2004). Applications of manganese-enhanced magnetic resonance imaging (MEMRI) to image brain plasticity in song birds. *NMR in Biomedicine, 8*, 602-612.

Venturi, G. (1973). Enzymatic activities and sodium, potassium and copper concentrations in mouse brain and liver after cuprizone treatment in vivo. *Journal of Neurochemistry, 21*, 1147-1151.

Wang, L., Li, H. J., & Zheng, W. (2008). Efflux of iron from the cerebrospinal fluid to the blood at the blood-CSF barrier: effect of manganese exposure. *Experimental Biology and Medicine, 233*, 1561-1571.

Watanabe, T., Frahm, J., & Michaelis, T. (2010). Myelin mapping in the living mouse brain using manganese-enhanced magnetization transfer MRI. *Neuroimage, 2*, 1200-1204.

WHO. (2012). *Micronutrient deficiencies*. Retrieved from World Health Organization: http://www.who.int/nutrition/topics/ida/en/index.html

Wolf, G. L., & Baum, L. (1983). Cardiovascular toxicity and tissue proton T1 response to manganese injection in the dog and rabbit. *American Journal of Roentgenology, 141*, 193-197.

Yamada, M. et a (2008). Diffusion-tensor neuronal fiber tractography and manganese-enhanced MR imaging of primate visual pathway in the common marmoset: preliminary results. *Radiology, 3*, 855-864.

Yin, Z., Jiang, H., Lee, E.-S. Y., Ni, M., Erikson, K. M., Milatovic, D., . . . Aschner, M. (2010). Ferroportin is a manganese-responsive protein that decreaseas manganese cytotoxicity and accumulation. *Journal of Neurochemistry, 112*(5), 1190-1198.

Yu, X., Nieman, B. J., Sudarov, A., Szulc, K. U., Abdollahian, D. J., Bhatia, N., . . . Turnbull, D. H. (2011). Morphological and functional midbrain phenotypes in Fibroblast Growth Factor 17 mutant mice detected by Mn-enhanced MRI. *Neuroimage, 3*, 1251-1258.

Zatta, P., Raso, M., Zambenedetti, P., Wittkowski, W., Messori, L., Piccioli, F., . . . Beltramini, M. (2005). Copper and zinc dismetabolism in the mouse brain upon chronic cuprizone treatment. *Cellular and Molecular Life Sciences, 62*, 1502-1513.

Zhang, N., Fitsanakis, V. A., Erikson, K. M., Aschner, M., Avison, M. J., & Gore, J. C. (2009). A model for the analysis of competitive relaxation effects of manganese and iron in vivo. *NMR in Biomedicine*, 391-404.

Zhang, S., Zhou, Z., & Fu, J. (2003). Effect on manganese chloride exposure on liver and brain mitochondria function in rats. *Brain Research, 93*, 149-157.

Zhao, F., Cai, T., Liu, M., Zheng, G., Luo, W., & Chen, J. (2009). Manganese induces dopaminergic neurodegeneration via microglial activation in a rat model of manganism. *Toxicological Sciences, 107*(1), 156-164.

Zheng, W., & Monnot, A. D. (2012). Regulation of brain iron and copper homeostasis by brain barrier systems: implication in neurodegenerative diseases. *Pharmacology & Therapeutics, 133*, 177-188.